THESIS FOR THE DEGREE OF DOCTOR OF PHILOSOPHY IN MATERIALS SCIENCE

Advancing Experimental, Modeling and Neural Network Techniques for Thixotropic Yield Stress Flows

Ases Akas Mishra

CHALMERS
UNIVERSITY OF TECHNOLOGY

Department of Mechanical Engineering
Chalmers University of Technology
Gothenburg, Sweden, 2026

Advancing Experimental, Modeling and Neural Network Techniques for Thixotropic Yield Stress Flows

Ases Akas Mishra

ISBN: 978-91-8103-362-5

Series number: 5819
ISSN 0346-718X
This thesis has been prepared using LaTeX.

Department of Mechanical Engineering
Chalmers University of Technology
SE-412 96 Gothenburg, Sweden
Phone: +46 (0)31 772 1000
www.chalmers.se

Printed by Chalmers Reproservice
Gothenburg, Sweden, February 2026

Abstract

Soft materials such as gels, suspensions, pastes, biological fluids, and polymers are central to a wide range of industrial, technological, and biological processes. Yet their flow behaviour remains exceptionally challenging to predict. In particular, thixo-elasto-viscoplastic (TEVP) fluids exhibit strong time-dependent restructuring, yielding, and viscoelasticity, making their response highly sensitive to measurement protocol, geometry, and flow history. Unlike Newtonian fluids, whose response is uniquely determined by instantaneous deformation, the behaviour of TEVP fluids reflects a time-dependent reorganization of their underlying microstructure under applied deformation. This temporal variability of the microstructure hampers model development, complicates process design, and limits the reliable use of TEVP soft materials in applications such as microfluidics, 3D printing, food processing, consumer product formulation, and biological lubrication. These challenges highlight the need for an integrated framework capable of linking microstructural dynamics, rheological response, and continuum-scale flow behaviour. This thesis develops such a unified framework by combining rheological characterization, flow-resolved imaging, continuum and structural-kinetic modeling, and data-driven neural network approaches to study TEVP materials across various shear histories in multiple flow geometries. First, rheological protocols are established to determine viscoelastic, viscoplastic, and thixotropic contributions in soft materials including Laponite suspensions, Carbopol gels, polymer blends, commercial yogurts, and human saliva. Flow behaviour is then investigated in confined geometries. Doppler Optical Coherence Tomography (D-OCT) measurements in rectangular millifluidic channels reveal plug regions, wall slip, shear localization, and scaling relationships linking rheological properties to velocity-field evolution. In circular pipes, transient pressure drop measurements are combined with structural kinetic modeling and continuum CFD simulations to

quantify the breakdown–recovery kinetics governing unsteady TEVP transport. To address limitations of classical constitutive models, neural network surrogates, including NARX network based digital rheometers and data-driven flow predictors, are trained on minimal experimental input. These models reconstruct full flow curves, predict transient rheological responses, and accurately capture unsteady pressure drop dynamics, helping resolve persistent issues of parameter identifiability and model selection. From a process engineering perspective, extrusion-based 3D printing is examined using rheology, dimensional analysis, and high-speed imaging to determine how elasticity, yield stress, and interfacial forces govern die swell, filament formation, and print fidelity. Complementary structural characterization using rheology coupled with scattering techniques (Rheo-SAXS) provides insight into flow-induced microstructural reorganization and its influence on die swelling. Finally, human saliva is examined as a biologically relevant thixotropic material. While its viscoelastic properties are well established, this work demonstrates and quantifies its clear thixotropic behaviour, identifying it as a detrimental factor in the perception of dry mouth (xerostomia). Together, these contributions advance a coherent experimental, computational, and data-driven methodology for TEVP materials, bridging continuum mechanics with microstructural origins and enabling more reliable prediction, process design, and formulation of soft materials across engineering and biomedical applications.

Keywords: Soft Matter, Thixotropy, Yield Stress, Scaling Laws, 3D Printing, Milifluidics, Structural Kinetic Modeling, Machine Learning.

Symbols and Abbreviations

Roman Symbols

A_{loop}, S_y	Hysteresis loop area (measure of thixotropy) [Pa·s^{-1}]
C_c	Carbopol concentration [wt.%]
C_p	Polyethylene oxide (PEO) concentration [wt.%]
D	Hydraulic diameter [m]
D_n	Needle/Nozzle diameter [m]
G'	Storage modulus [Pa]
G''	Loss modulus [Pa]
H	Duct height [m]
h	Duct half-height [m]
$I(q)$	Radially Integrated azimuthal scattering intensity (SAXS)
K_1, K_2	Equation of state coefficients
k_1, k_2	Kinetic equation coefficients
L_{DS}	Die swell position [m]
$\dot{M}$	Mass flow rate [kg/s]
Q	Volumetric flow rate [m^3/s]
R	Pipe radius [m]
t	Time [s]
U	Velocity [m/s]
u_s	Slip velocity [m/s]
$V_{\max}$	Maximum inlet velocity [m/s]
W	Duct width [m]
W_{DS}	Die swell width [m]
W_p	Print width [m]

x, y, z	Cartesian coordinates
$y(t)$	Target output (shear stress time series)
$\hat{y}(t)$	Predicted shear stress
$u(t)$	Input signal (shear rate time series)
w_{ij}	Neural network weights
b_i	Bias terms in neural network layers
n_h	Number of hidden neurons

Greek Symbols

$\dot{\gamma}$	Shear rate [s^{-1}]
σ	Shear stress [Pa]
σ_y	Yield stress [Pa]
σ_{ST}	Surface tension [N/m]
η	Shear viscosity [Pa·s]
η^+	Transient shear viscosity [Pa·s]
τ_w	Wall shear stress [Pa]
ρ	Density [kg/m^3]
λ	Structural parameter
ν	Kinematic viscosity [m^2/s]
ω	Angular frequency [rad/s]
ΔP	Pressure drop [Pa]
$\Delta\omega$	Doppler frequency shift [Hz]
Φ	Volume fraction [%]
ϕ	Phase angle [rad]

Dimensionless Numbers

Re	Reynolds number: $Re = \dfrac{\rho U D}{\eta}$
Bi	Bingham number: $Bi = \dfrac{\sigma_y}{\eta\dot{\gamma}}$
Bi^*	Modified Bingham number: $\dfrac{\xi}{Bi} = \dfrac{\eta\dot{\gamma}G'}{\sigma_y^2}$
Oh	Ohnesorge number: $Oh = \dfrac{\eta}{\sqrt{\rho\sigma_{ST}D_n}}$
Tx	Thixotropy number: $Tx = \dfrac{A_{\text{loop}}}{\eta\dot{\gamma}}$

Abbreviations

ANN	Artificial Neural Network
CFD	Computational Fluid Dynamics
CC	Concentric Cylinder (rheometer geometry)
CLS	Confocal Laser Scanning Microscopy
D-OCT	Doppler Optical Coherence Tomography
DNS	Direct Numerical Simulation
ESEM	Environmental Scanning Electron Microscopy
EVP	Elasto-Viscoplastic
IKH	Isokinetic Herschel–Bulkley model
LDA	Laser Doppler Anemometry
MITT	Multi-Interval Thixotropy Test
MMW	Moore–Mewis–Wagner model
MRV	Magnetic Resonance Velocimetry
NARX	Nonlinear Autoregressive model with Exogenous input
PINN	Physics-Informed Neural Network
PEO	Polyethylene Oxide
PIV	Particle Image Velocimetry
PTV	Particle Tracking Velocimetry
RhINN	Rheology-Informed Neural Network

SAXS	Small Angle X-ray Scattering
SKM	Structural Kinetic Model
TEVP	Thixo-Elasto-Viscoplastic
UVP	Ultrasound Velocity Profiling
YSF	Yield Stress Fluid

Contents

CHAPTER 1

Introduction

1.1 Background of the Research Project

Soft matter systems, particularly thixotropic and yield stress materials, are central to industries including food processing, consumer products, health care, construction, and manufacturing. They also play a role in natural phenomena such as avalanches, mudflows, and debris transport. Yet their flow behaviour remains notoriously difficult to predict [1], [2], [3]. Even quantities such as the yield stress or the pressure gradient required to initiate flow can depend strongly on measurement technique, boundary conditions, microstructural state, and flow history [4]. This lack of reproducibility and the absence of coherent modeling frameworks force many industrial processes to rely on trial-and-error design, leading to inefficiencies, safety concerns, and elevated costs.

The challenge stems from the inherently multi-scale nature and time depen-

dency of thixo-elasto-viscoplastic (TEVP) materials [2], [5]. Their rheological response depends not only on instantaneous deformation but also on their evolving microstructure. Yielding, thixotropy, and viscoelasticity often coexist, giving rise to complex behaviours such as plug flow, delayed yielding, transient overshoots, wall slip, and hysteresis. Traditional constitutive models attempt to capture these features but frequently fail because they rely on (i) oversimplified microstructural assumptions, (ii) poorly constrained or unmeasurable parameters, and (iii) limited experimental observables. Consequently, no widely accepted framework exists to determine which combination of measurements and constitutive models is appropriate in a given scenario, a central issue identified across academia and industry [6].

At the same time, engineering practice increasingly demands predictive control of soft matter flows, because the underlying material behaviour directly governs flow stability, energy consumption, product uniformity, and overall process reliability [1]. This need is especially evident in extrusion and processing flows, where TEVP behaviour governs pressure build-up, die swell, flow instabilities, and final product quality [7], [8]; in food, pharmaceutical, and consumer-product manufacturing, where transient rheology dictates texture, stability, and processability [9]; and in microfluidic and biomedical contexts, where geometric confinement magnifies the consequences of time-dependent yielding and structural evolution [10]. These industrial and societal needs call for new multidisciplinary strategies that integrate advanced rheological characterization, spatially resolved flow measurements, data-driven and physics-based modeling, and machine learning-based prediction.

1.2 Outline of the Thesis

The overarching goal of this thesis is to develop a unified experimental, computational, and data-driven framework for understanding and predicting the

flow behaviour of TEVP soft materials. These materials, ranging from suspensions to polymer gels, food materials, and biologically relevant fluids, exhibit strongly time-dependent, nonlinear rheology driven by the progressive, flow-induced reconfiguration of their internal microstructure. Their behaviour is emblematic of yield stress materials (YSMs) more broadly, which flow only above a critical stress and otherwise behave as solids.

Motivated by long-standing challenges in the rheology and modeling of time-dependent and YSMs, the objectives of this thesis are to advance the state-of-the-art in the field by

A. quantifying the rheological signatures of TEVP behaviour through controlled experiments,

B. link these signatures to flow fields in several geometries using flow measurements and advanced imaging techniques,

C. develop predictive models that incorporate structural kinetics and structure-informed constitutive behaviour, and

D. establish data-driven neural network approaches capable of reconstructing rheological functions and transient responses from minimal experimental input.

Naturally, taken together, these objectives go beyond the scope of one single PhD thesis. However, within the materials and industrial applications of interest, the thesis contributes toward the broader vision of reducing the gap between measured and predicted material behaviour by combining experimentation, modeling, and data science into a coherent predictive framework. Specifically:

- **Rheological characterization:** The viscoelasticity, yield stress, and thixotropy of model and industrial soft materials were quantified using steady shear and oscillatory rheological experiments (objective **A.**).

These measurements provide the material functions that characterize microstructural breakdown, recovery, yielding and viscoelastic contributions, addressing the need for more reliable and reproducible rheological protocols.

- **Flow behaviour in confined geometries:** Using flow measurements and more advanced tomographic techniques, temporally and spatially resolved flow fields were obtained in circular tubes and rectangular millifluidic channel geometries (objective **B.**). In millifluidic channels these experiments reveal plug regions, wall slip, and shear localization, thus connecting rheological signatures to real flow behaviour using novel scaling laws. Complementary computational fluid dynamics (CFD) modeling of pipe flow, elucidate transient pressure drops and microstructural evolution during unsteady transport of soft matter (objective **C.**).

- **Neural network-based rheology and flow prediction:** To overcome limitations of traditional constitutive models, data-driven rheological frameworks were developed using neural networks trained on minimal experimental input (objective **D.**). These networks reconstruct full flow curves, predict transient shear responses, and act as digital rheometers capable of generalizing across deformation histories. Neural network predictions of flow dynamics dramatically reduce computational cost while retaining high accuracy, contributing to the development of efficient predictive tools suitable for real world applications.

- **Extrusion and 3D printing of polymer blends:** Experiments combining rheology, high-speed imaging, and structural characterization using scattering techniques were conducted to identify how viscoelasticity, yield stress, and interfacial forces govern die swell, filament formation, and print fidelity. These results address relevant questions concerning the link between microstructure, flow kinematics, and print performance

in extrusion-based manufacturing (objective **B.**).

- **Bio-based soft matter rheology:** Human saliva serves as a biologically relevant soft material whose rheological behaviour remains poorly characterized. Through careful rheological analysis, its thixotropic nature was revealed, and scaling laws were established that link its flow dynamics to its rheological functions, offering new insight into the physical origins of xerostomia (the sensation of dry mouth) (objective **A.**).

1.3 Continuum Mechanics and the Structural Origins of Nonlinear Rheology

Nonlinear rheology refers to regimes in which the stress is no longer proportional to the applied deformation or shear rate, resulting in a nonlinear constitutive relation between stress and shear rate, often accompanied by flow-induced microstructural evolution [7]. Understanding the flow behaviour of complex fluids requires an appreciation of a fundamental duality: on the one hand, a *continuum mechanics description*, in which materials are characterized through bulk quantities such as stress, viscosity, and other material functions; and on the other hand, a *material structural perspective*, in which the microscopic or mesoscopic organization of the material determines how these bulk quantities evolve under flow. Keeping both pictures in mind is essential for interpreting the nonlinear rheological phenomena examined later in this thesis.

From a continuum point of view, the central task is to specify the functional form of constitutive relations. For TEVP materials, this involves introducing constitutive functions that depend explicitly on shear rate and time. Within such a framework, thixotropy naturally emerges as the behaviour of a fluid whose viscosity decreases or increases depending on the flow history. This description often motivates the introduction of a structural parameter that

evolves dynamically, providing a compact way to encode how material functions depend on deformation and time.

However, adopting only the continuum viewpoint leaves open a natural question: what kinds of materials actually exhibit such behaviour, and why? This leads to the second aspect of the duality, namely the material structural origins of nonlinear rheology. Despite the unifying power of continuum theory, real complex fluids possess a wide variety of microstructures, dispersed particles, gels, entangled polymers, emulsions, and biological assemblies, each with its own characteristic structural response to flow / deformation. What soft matter systems share is that their internal structure can be significantly altered by externally imposed flow fields. Thus, flow modifies structure, and the material structural response in turn modulates the flow field [11].

The remainder of the theoretical framework in this thesis builds on this dual perspective. The continuum description provides the mathematical formulation needed for predicting flows in simple shear. The structural viewpoint explains why phenomena such as viscoelasticity, shear thinning, yielding, and thixotropy occur, and why they differ across materials with distinct microstructures. Together, these complementary approaches clarify both the origins and implications of the nonlinear rheology observed throughout the thesis.

1.4 Rheological Properties Relevant to this Thesis

Viscoplasticity

Yield stress is a critical material property that defines the threshold at which a material transitions from a solid-like to a fluid-like behaviour under applied stress [12], [13], [14]. This phenomenon is observed in a variety of soft matter, such as gels, pastes, foams, and suspensions [15]. Thus, the yield stress represents the critical stress required to initiate plastic deformation in a material.

In a material without a yield stress, such as a Newtonian fluid, any applied stress results in continuous flow, with no defined threshold for deformation.

From a material point of view, the yielding dynamics can be understood in terms of structural rearrangements. Below the yield stress, the material's microstructure is typically in a metastable state, where particles, colloidal clusters, or polymer chains are trapped in energy basins. These basins correspond to configurations that resist deformation due to intermolecular interactions, such as Van der Waals forces, ionic bonds, or entanglements [4], [13]. When the applied stress reaches the yield stress, these interparticle forces are overcome, and the system undergoes a local rearrangement, triggering the onset of plastic deformation. In colloidal suspensions, for example, the yield stress corresponds to the stress required to break the confinement of particles that are held in place by attractive forces or steric interactions. As the yield stress is exceeded, particles start to rearrange, and the material exhibits flowing behaviour. This process can involve the breaking of interparticle bonds, the disentangling of polymer chains, or the unclustering of aggregates, depending on the system. In gels and solid-like materials, yielding is often associated with the breaking of network structures. These networks, formed by crosslinked polymers or colloidal particles, provide structural integrity to the material. At yield, the network undergoes breakdown or disruption, and the material transitions to a more fluid-like state [2].

Yield stress is lengthscale-dependent and can vary with the size of the material structures being deformed. In nanoparticle systems, for instance, the yield stress can be influenced by the aggregation state of the nanoparticles, where larger aggregates require higher stresses to break. Similarly, in polymer gels, the crosslink density and molecular weight of the polymer chains affect the yield stress, as denser networks or longer chains can resist deformation more effectively. At the macroscale, yield stress is affected by boundary conditions, such as the rate of applied stress and the sample's geometry. For example,

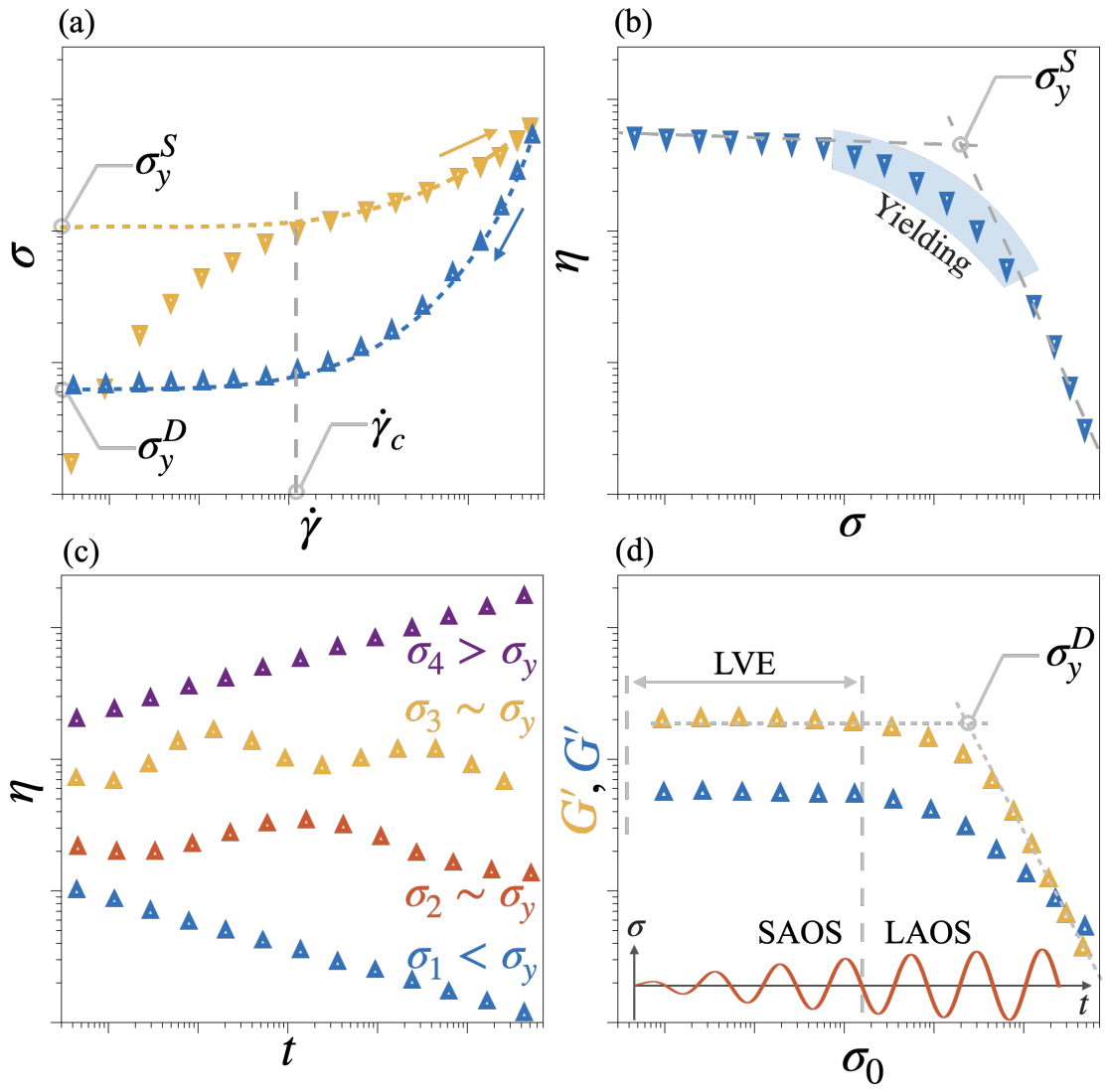

Figure 1.1: Overview of rheological methods for determining yield stress. (a) Rate-controlled steady shear tests showing upward and downward shear rate ramps fitted with viscoplastic models to estimate σ_y^S and σ_y^D, respectively. (b) Stress-controlled steady shear tests where viscosity decreases once σ exceeds the yield range. (c) Creep tests illustrating solid-like response below yield, flow above yield, and competing breakdown/re-aggregation near the yield stress. (d) Stress-controlled oscillatory tests showing the transition from linear viscoelasticity (SAOS) to LAOS regime and the decrease in moduli used to infer σ_y^D.

slower deformation rates often result in lower yield stresses because the system has more time to rearrange before yielding. Yield stress also depends on the timescale of the applied shear. For slow deformations (long timescales), materials may show significant strain hardening before yielding, where the material's resistance to flow increases over time due to structural rearrangements. On faster timescales, the material may behave more like a viscous fluid, with a yield stress that depends primarily on the material's flow properties rather than its internal structure [2], [15].

In soft jammed systems dominated by repulsive interactions, dispersed elements become geometrically confined at high volume fractions, forming a percolated network that stores elastic energy when deformed; in these materials, solidity arises from crowding rather than bonding, and the yield stress reflects the stress required to trigger irreversible rearrangements that push elements out of their trapped configurations [4], [12]. By contrast, in aggregated systems where attractive forces dominate, solidity derives from particle to particle bonds formed through van der Waals attractions, polymer bridging, or electrostatic interactions, and yielding corresponds to breaking this load bearing network; the yield stress therefore reflects the strength of interparticle interactions, and because the network can rebuild over time, these materials often exhibit thixotropy with structure recovery at rest and breakdown under shear [2], [16].

In practice, two definitions of the yield stress are common: static (σ_y^S) and dynamic (σ_y^D) yield stresses represent the stress required to initiate and maintain flow, respectively [17], [18], [19]. Measuring the yield stress is not straightforward due to the material's nonlinear behaviour, especially in thixotropic yield stress materials. Several rheological tests have been developed to estimate the yield stress, each applicable to different material types and testing conditions [20]. Common techniques include:

- **Rate controlled steady shear test** (Fig. 1.1(a)): In this test, a

shear rate ($\dot{\gamma}$) ramp down is imposed and the resulting shear stress (σ) is measured. The flow curve ($\sigma(\dot{\gamma})$) is typically fitted with viscoplastic constitutive models (e.g., Herschel-Bulkley) to estimate the dynamic yield stress σ_y^D by extrapolation to $\dot{\gamma} \to 0$ (blue curve in Fig. 1.1(a)). If a stress ramp up is performed, the viscoplastic model fitting gives an estimate of the static yield stress (σ_y^S) (yellow curve in Fig. 1.1(a)). For modeling purposes, the critical shear rate ($\dot{\gamma}_c$) where the material yields corresponds to the point on the abscissa where the model deviates from the experimental dataset [17]. Note that, the deviation between the upward and downward shear rate ramp curves is observed only for thixotropic yield stress fluids, whereas for the so-called simple yield stress fluids both curves superimpose.

- **Stress controlled steady shear test** (Fig. 1.1(b)): Here, the applied stress (σ) is gradually increased while the apparent viscosity is measured. For $\sigma < \sigma_y^S$, the material behaves as an elastic solid with high apparent viscosity. When $\sigma \geq \sigma_y^S$, a pronounced decrease in viscosity occurs, indicating structural breakdown and transition to plastic deformation [13]. This method highlights that yielding is gradual and may span over a stress range (blue shaded region in Fig. 1.1(b)) rather than occurring at a single point.

- **Creep test** (Fig. 1.1(c)): In a creep test, a constant stress is applied and the viscosity is measured over time. If the stress is below σ_y, the material behaves as a solid and the viscosity increases with time due to Brownian rearrangements. If the stress is above σ_y, the structure breaks down initiating flow, marked by a decrease in viscosity with time. For stresses near σ_y, structural breakdown competes with gradual structural re-aggregation, resulting in a fluctuation of the viscosity function [18].

- **Stress controlled oscillatory test** Fig. 1.1(d): σ_y^D can be measured

from oscillatory tests by performing a shear stress ramp and measuring the dynamic moduli (G', G''). In the small amplitude oscillatory shear (SAOS) regime, the dynamic moduli remain independent of the applied strain amplitude, reflecting the linear viscoelastic (LVE) region. Subsequent increase of stress in the large amplitude oscillatory shear (LAOS) regime results in a nonlinear behaviour, marked by a decrease in dynamic moduli and the onset of yielding as the microstructure can no longer fully recover. Intersection of the tangents drawn on the storage modulus (G') curve (usually) gives an estimate of σ_y^D. However, in some studies the crossover point of the dynamic moduli has been taken as the yield stress [17], [21]. From a nonlinear oscillatory shear perspective, this description is oversimplified, as the dynamic yield stress inferred from oscillatory moduli depends on the chosen oscillation frequency and associated time scale.

Viscoelasticity

Viscoelasticity refers to the dual solid- and liquid-like response of materials whose microstructural elements provide elastic resistance but are able to relax and rearrange either over characteristic timescales or under sufficiently large deformations [1], [22], [23]. Viscoelasticity can be probed under shear, extensional, or oscillatory deformations. Here we focus on oscillatory shear, where the linear small amplitude oscillatory shear (SAOS) regime provides a convenient means to resolve the elastic and viscous contributions. In SAOS, the material is subjected to a sufficiently small sinusoidal strain amplitude (γ_0) with an angular frequency ω, typically written as $\gamma(t) = \gamma_0 \sin(\omega t)$, and the resulting stress response remains sinusoidal but phase-shifted (stress amplitude σ_0 and phase angle δ), $\sigma(t) = \sigma_0 \sin(\omega t + \delta)$, due to the combined solid- and liquid-like behavior. From this response, the storage modulus, $G' = (\sigma_0/\gamma_0)\cos\delta$, and the loss modulus, $G'' = (\sigma_0/\gamma_0)\sin\delta$, quantify the elastic energy stored

and viscous energy dissipated, respectively. The SAOS regime is useful for characterizing the quiescent structure because the deformation is too small to induce irreversible structural rearrangements, consistent with standard linear viscoelasticity frameworks such as the Maxwell and Kelvin-Voigt models. Soft materials such as gels, emulsions, colloidal glasses, and polymer or micellar networks often display fluid-like behaviour at low frequencies and solid-like behaviour at high frequencies, reflecting their broad spectrum of internal relaxation processes. However, when the imposed oscillatory strain amplitude increases (transition to large amplitude oscillatory shear, LAOS), the material enters a nonlinear regime in which the structure is progressively and irreversibly deformed, realigned, or broken [24], [25]. In this regime, the stress response is no longer purely sinusoidal and higher harmonics appear in the corresponding Fourier spectra of the time-dependent shear stress response. As illustrated in Fig. 1.2(a), the SAOS regime is marked by strain–independent moduli and a purely sinusoidal stress response (Fig. 1.2(b)), reflected in the elliptical Lissajous curves in the $\sigma(t) - \gamma(t)$ plane (Fig. 1.2(d)). As the strain amplitude increases into the nonlinear regime, the moduli begin to deviate from their linear values, the stress waveform becomes increasingly distorted (Fig. 1.2(c)), and the corresponding Lissajous curves develop pronounced nonlinear features (non-elliptic loops) Fig. 1.2(d).

Many soft matter systems deform through intermittent, localized rearrangements of small clusters of particles or segments, often referred to as shear transformation zones (STZs) [26], [27]. These plastic events reorganize stress across the material through long-range elastic fields, and when they proliferate and begin to interact, the material approaches yielding. Such rearrangements can occur across length scales depending on the system, but the phenomenology is universal, i.e. small reversible distortions give way to irreversible cage breaking, bond stretching, and network rupture as strain increases. The SAOS to LAOS transition is highly sensitive to changes in material structure and per-

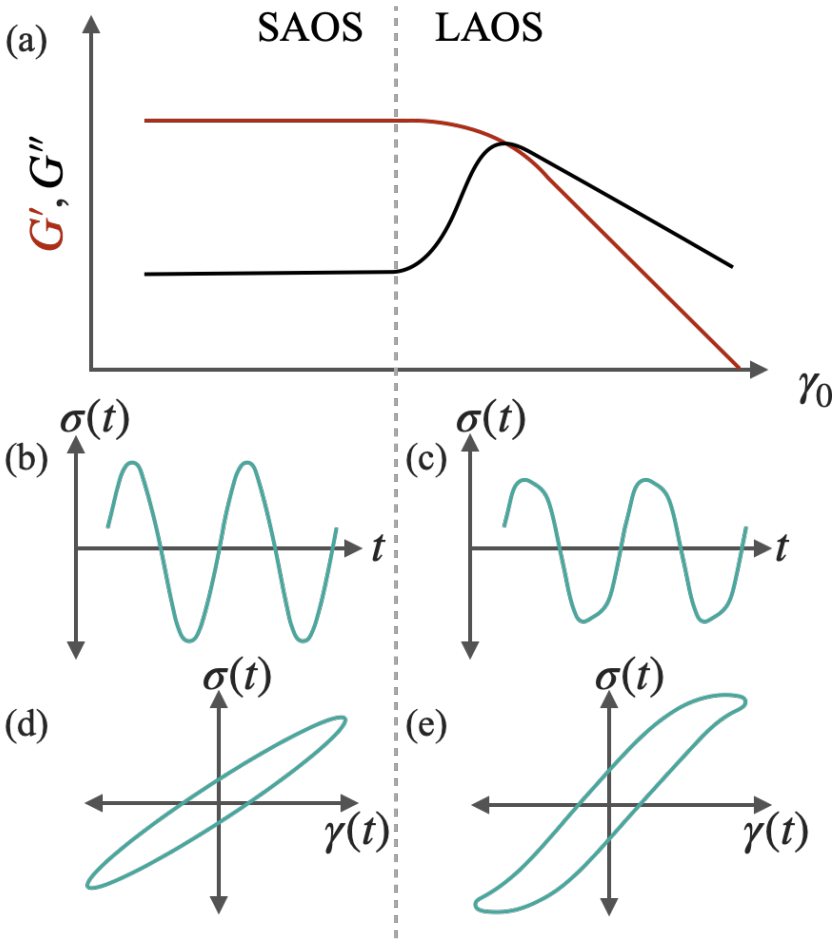

Figure 1.2: Illustration of the transition from linear (SAOS) to nonlinear (LAOS) oscillatory shear. In SAOS, the moduli are strain-independent and the stress response is purely sinusoidal, whereas in LAOS, the waveform distorts, and nonlinear Lissajous curves emerge.

mits soft materials to be grouped into four characteristic response types, in common practice. [28].

- **Type I** (strain thinning) occurs when both G' and G'' decrease monotonically with strain, often due to alignment or disentanglement of flexible microstructures, as in many polymer melts or polymer solutions.
- **Type II** (strain hardening) shows simultaneous increases in both moduli, typically arising in systems where deformation promotes association or network tightening.

- **Type III** (weak strain overshoot) is characterized by an overshoot of G'' as structure transiently resists flow before yielding. This occurs when moderate rearrangements release stored stress without full network rupture.

- **Type IV** (strong strain overshoot) involves pronounced peaks in both G' and G'', signaling cooperative structural alignment followed by rapid collapse, commonly seen in highly interconnected gels or aggregated colloidal networks.

Thermodynamically, these transitions reflect the competition between elastic energy storage and dissipation through irreversible configurational rearrangements. At low strain, deformation occurs within a single free-energy basin. At larger strain, the material is driven across energy barriers into new metastable states, enabling flow. The location and sharpness of the overshoot thus encode the energy landscape of the microstructure: weak overshoots indicate shallow barriers and loosely connected networks, while strong overshoots indicate deep barriers and highly reversible elastic loading before abrupt yielding [23], [26], [28].

Viscoelastic behaviour can be understood using simple mechanical analogs composed of springs and dashpots [29]. A spring represents ideal elasticity: it deforms instantly under stress and fully returns to its original state when the stress is removed, storing mechanical energy in the process. A dashpot, in contrast, represents ideal viscosity: it flows continuously under stress and does not recover, dissipating energy as heat. Combining these elements allows us to model the viscoelastic response of soft materials. In a creep and recovery test, where a constant stress is applied and later removed (Fig. 1.3(A0)), an ideal elastic solid shows an immediate strain that is fully recovered upon unloading (Fig. 1.3(A1)), while a Newtonian fluid exhibits continuously increasing strain that remains after the imposed stress is removed (Fig. 1.3(A2)). A

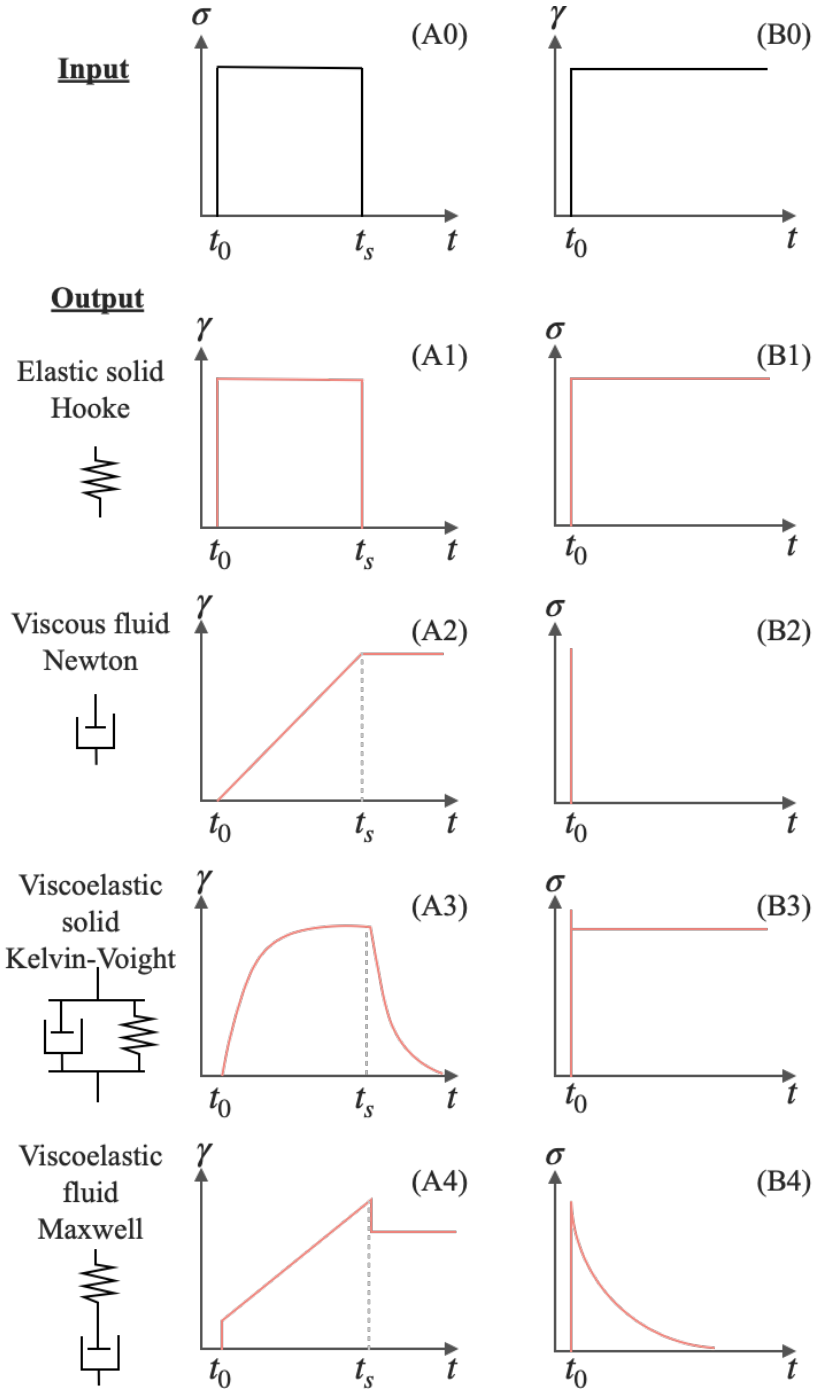

Figure 1.3: Creep–recovery (A0–A4) and stress-relaxation (B0–B4) responses of ideal elastic, viscous, and viscoelastic materials modeled using spring (elastic) and dashpot (viscous) elements. In the creep–recovery tests (A0), an elastic solid shows instantaneous and fully recoverable strain (A1), a viscous fluid flows irreversibly (A2), a Kelvin–Voigt solid creeps and then slowly recovers (A3), and a Maxwell fluid exhibits both instantaneous elastic deformation and permanent flow (A4). In the stress-relaxation tests (B0), the elastic solid maintains constant stress (B1), the viscous fluid relaxes immediately (B2), the Kelvin–Voigt solid relaxes to an elastic plateau (B3), and the Maxwell fluid displays exponential stress decay (B4).

Kelvin–Voigt viscoelastic solid (spring and dashpot in parallel) gradually approaches a finite strain during creep and slowly returns to zero strain during recovery, reflecting temporary deformation stored in the spring and resisted by the dashpot (Fig. 1.3(A3)). A Maxwell viscoelastic fluid (spring and dashpot in series) displays an initial elastic deformation followed by viscous flow, so only the elastic portion is recovered upon unloading (Fig. 1.3(A4)). The complementary stress relaxation test, where a sudden strain is imposed (Fig. 1.3(B0)), further distinguishes these responses: an elastic solid holds constant stress (Fig. 1.3(B1)), a viscous fluid relaxes immediately (Fig. 1.3(B2)), a Kelvin–Voigt solid relaxes rapidly to an elastic plateau (Fig. 1.3(B3)), and a Maxwell fluid exhibits exponential stress decay (Fig. 1.3(B4)).

Thixotropy

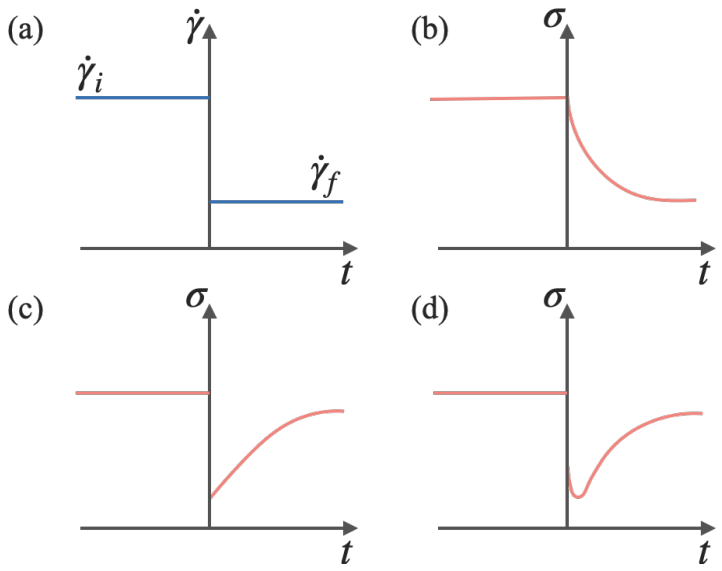

Figure 1.4: Schematic comparison of viscoelastic and thixotropic responses to a step decrease in shear rate. (a) Imposed step from an initial shear rate $\dot{\gamma}_i$ to a lower shear rate $\dot{\gamma}_f$. (b) Purely viscoelastic materials exhibit a monotonic stress relaxation to the new steady state. (c) Thixotropic materials show an instantaneous stress drop followed by slow structural rebuilding. (d) In the general case, the measured stress combines fast viscoelastic relaxation with slower thixotropic recovery, the latter distinguishing true thixotropy.[29]

Thixotropy is a reversible, time-dependent decrease of viscosity under flow and recovery when flow ceases. Thixotropy arises from flow-induced, reversible structural changes [12], [30], [31]. In attractive colloids, weak interparticle forces (van der Waals, H-bonding, or polymer-mediated bridging/depletion) form flocs and percolated networks at rest. Hydrodynamic stresses during flow break and refine these structures, decreasing viscosity. Reversing or stopping flow allows re-aggregation and network rebuild at finite timescales [32], [33], [34]. Flocs are often fractal over a range of scales, and increasing shear typically reduces floc size and can densify weak flocs (changing fractal dimension). At low shear, orthokinetic flocculation can compete with breakup [3], [30].

Both viscoelastic and thixotropic materials show time and history effects

(e.g., shear-thinning, hysteresis, start-up overshoots), so these signatures alone do not uniquely identify thixotropy. The decisive experiment is a step-down in shear rate (Fig. 1.4(a)), wherein viscoelastic materials show a monotonic relaxation of stress to the new steady state that depends only on their relaxation spectrum and does not involve structural rebuilding (Fig. 1.4(b)). Whereas, thixotropic materials typically show an instantaneous drop in stress, followed by a slow, time-dependent recovery or evolution due to microstructural regeneration (Fig. 1.4(c)). In the most general case, the measured stress response contains both a fast viscoelastic relaxation and a slower thixotropic structural recovery (Fig. 1.4(d)), the latter being the signature that distinguishes thixotropy from purely viscoelastic behaviour [30].

Reversibility must be demonstrated using carefully designed shear histories. Apparent irreversibility does not necessarily indicate non-thixotropic behaviour, as it may result from incomplete dispersion, physical or chemical aging, or path-dependent transitions between non-equilibrium microstructural states.

Thixotropy is commonly measured using the following rheological tests:

- **Hysteresis loops (shear rate ramps):** Ascending/descending shear rate sweeps produce a loop because stress evolution lags structural evolution [35]. Loop area/shape depends strongly on shear history, ramp rate, and the maximum shear rate. Variants of hysteresis loop include overshoot-dominated loops, self-intersecting loops, and loops influenced by shear-banding at low shear (identified by stress plateaus). Time and shear rate are coupled in this test (Fig. 1.5(a)).

- **Start-up flow and creep test:** In start-up flow (Fig. 1.5(b), $\sigma - t$), a material at rest is suddenly sheared at a constant shear rate, producing a stress overshoot (σ_{OV}) followed by decay to steady state (σ_{SS}). The overshoot reflects the breakdown of the rested microstructure, making it

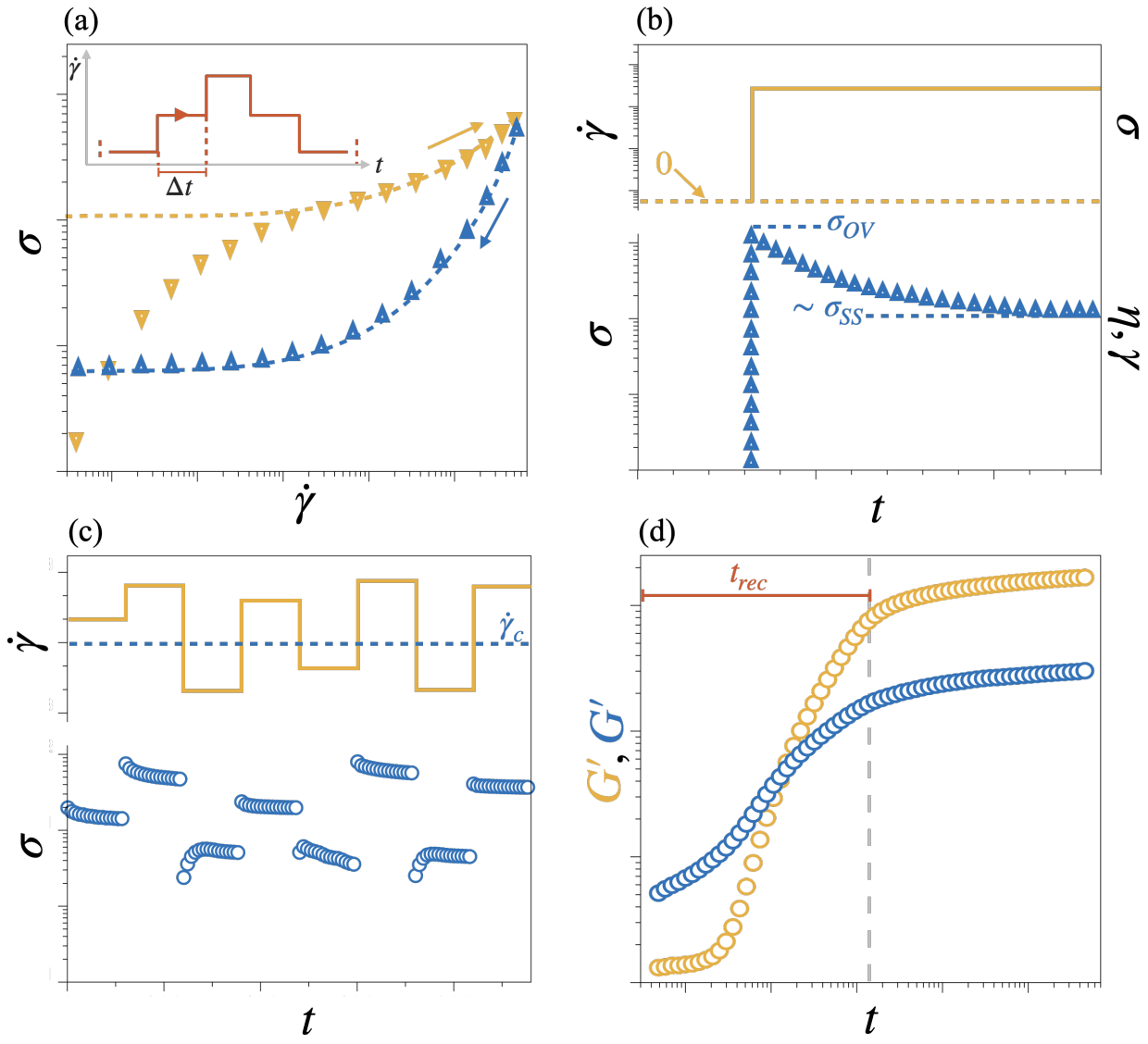

Figure 1.5: Representative rheological tests used to probe thixotropy: (a) Hysteresis loops from shear-rate ramps, (b) start-up flow (left axis) showing stress overshoot and relaxation, and creep (right axis) showing strain/viscosity evolution with time, (c) step changes in shear rate (3ITT/MITT) highlighting breakdown and recovery, (d) SAOS recovery tracking microstructural rebuilding through time-dependent dynamic moduli.

a useful measure of structural recovery/relaxation time. This method is destructive, since each start-up resets the structure and must be repeated for each condition. The overshoot is not a fixed yield stress and can vary with shear rate. In a creep test, a constant stress is applied and the strain or viscosity is monitored over time (Fig. 1.5(b), $\gamma - t$ or $\eta - t$). Below the yield stress, the strain reaches a finite plateau and is fully recovered once the stress is removed. Above the yield stress, the strain rate gradually accelerates to a steady flow. In thixotropic materials, the response is strongly history-dependent, and creep curves can become complex, especially near the dynamic yield stress: the strain may initially level off, then begin to flow after a delay that shortens as the stress increases [13].

- **Step change in shear rate:** Step-change tests avoid the limitations of hysteresis loops by imposing sudden changes in shear rate after the material has first been brought to a steady state, ensuring reproducible initial conditions. When the shear rate is stepped up above the critical yielding shear rate ($\dot{\gamma}_c$), the stress response decreases with time due to structural breakdown. However, when the shear rate is stepped down below $\dot{\gamma}_c$, the time-dependent increase in stress reflects the rebuilding of microstructure and provides one of the clearest signatures of thixotropy. Because time and shear rate can be varied independently, these tests are well suited for evaluating thixotropy models. Step-up and step-down tests should be performed across a wide range of shear rates to fully characterize thixotropic behaviour. Variants of this test include the Three-Interval Thixotropic Test (3ITT) and the Multi-Interval Thixotropic Test (MITT) (Fig. 1.5(c)) [36].

- **Oscillatory test:** Thixotropic recovery at rest and rheological gel formation ($G' > G''$) can be monitored non-destructively by performing

a SAOS test at a constant strain amplitude in the LVE regime, which probes the evolving microstructure without significantly perturbing it. The time evolution of the dynamic moduli, particularly the development of dynamic moduli plateaus with time, reflects network rebuilding (Fig. 1.5(d)). However, long recovery times (often hours to days) can make it difficult to distinguish reversible thixotropic recovery from irreversible aging or slow aggregation [16].

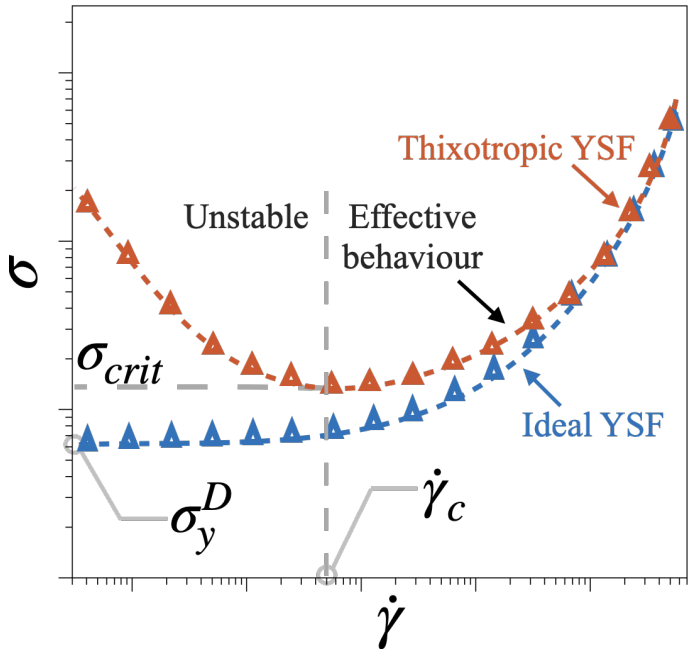

Figure 1.6: Schematic constitutive flow curve of a thixotropic yield stress fluid compared to an ideal yield stress fluid.

The flow curve of a thixotropic yield stress fluid differs from that of an ideal yield stress fluid because the material's internal structure continually evolves with time, Fig. 1.6. At low shear rates, the applied deformation is too weak to break down the microstructure. For a thixotropic yield stress fluid sheared below the critical shear rate ($\dot{\gamma}_c$), strong elastic effects together with structural

rejuvenation driven by Brownian motion lead to continued structural build-up. As a result, the viscosity increases and the shear stress decreases with increasing shear rate until a critical stress, σ_{crit}, is reached. This produces a non-monotonic and unstable region in the flow curve, where homogeneous flow cannot be sustained, leading to flow stoppage. At higher shear rates, structural breakdown dominates, resulting in an increase in stress characteristic of shear thinning fluids. In contrast, for a simple yield stress fluid, the stress plateaus at low shear rates (dynamic yield stress, σ_y^D), and shear thinning behaviour dominates at higher shear rates. The effective flow curve of a thixotropic yield stress fluid therefore arises from the competition between the unstable stress decrease at low shear rates ($\dot{\gamma} < \dot{\gamma}_c$) and the low-shear plateau characteristic of simple yield stress fluids.

1.5 Continuum Modeling

Governing Equations

The motion of a homogeneous, incompressible, and isothermal fluid is governed by the Cauchy momentum equation together with the incompressibility constraint. Using bold lowercase symbols for vectors and bold uppercase symbols for tensors, these read

$$\nabla \cdot \mathbf{u} = 0, \tag{1.1}$$

$$\rho \frac{D\mathbf{u}}{Dt} = \nabla \cdot \mathbf{S} + \mathbf{f}_B, \tag{1.2}$$

where $\mathbf{u}$ is the velocity field, ρ is the density, $\mathbf{f}_B$ denotes body forces per unit volume, and $\mathbf{S}$ is the Cauchy stress tensor.

The material derivative of the velocity can be written using the velocity gradient tensor

$$\mathbf{L} = \nabla \mathbf{u}, \tag{1.3}$$

so that

$$\frac{D\mathbf{u}}{Dt} = \frac{\partial \mathbf{u}}{\partial t} + \mathbf{L}\,\mathbf{u}. \tag{1.4}$$

The velocity gradient tensor admits the unique decomposition

$$\mathbf{L} = \mathbf{D} + \mathbf{W}, \tag{1.5}$$

where

$$\mathbf{D} = \tfrac{1}{2}\left(\mathbf{L} + \mathbf{L}^{\mathsf{T}}\right), \qquad \mathbf{W} = \tfrac{1}{2}\left(\mathbf{L} - \mathbf{L}^{\mathsf{T}}\right), \tag{1.6}$$

are the rate–of–deformation (symmetric) and spin/vorticity (antisymmetric) tensors, respectively. The Cauchy stress is written as the sum of an isotropic pressure contribution and an extra-stress tensor,

$$\mathbf{S} = -p\,\mathbf{I} + \mathbf{T}_E, \tag{1.7}$$

where p is the isotropic pressure and $\mathbf{I}$ is the identity tensor.

For a Newtonian fluid, the extra-stress tensor depends linearly on the deformation rate,

$$\mathbf{T}_E = 2\eta\,\mathbf{D}, \tag{1.8}$$

where η is the dynamic viscosity. Substituting this constitutive relation into Eq.1.2 yields the incompressible Navier-Stokes equations:

$$\rho\left(\frac{\partial \mathbf{u}}{\partial t} + \mathbf{u}\cdot\nabla\mathbf{u}\right) = -\nabla p + \eta\nabla^2\mathbf{u} + \mathbf{f}_B. \tag{1.9}$$

A scalar measure of the local shear rate is provided by the second invariant of the tensor $\mathbf{D}$,

$$\dot{\gamma} = \sqrt{2\,\mathbf{D}:\mathbf{D}}, \tag{1.10}$$

where ":" denotes the double tensor contraction, which expressed in terms of the trace of the tensor is $\mathbf{D}:\mathbf{D} = \mathrm{tr}(\mathbf{D}^2)$.

Many fluids of practical relevance exhibit non-Newtonian behaviour such as shear thinning, viscoelasticity, viscoplasticity, and thixotropy. In such cases, more advanced constitutive relations must be employed [7]. For thixotropic fluids, the apparent viscosity depends not only on the instantaneous shear rate but also on an internal structural parameter $\lambda \in [0, 1]$ describing the evolving microstructure. A generalized 1D constitutive relation may be written as

$$\mathbf{T}_E = 2\,\eta_{\text{eff}}(\dot{\gamma}, \lambda)\,\mathbf{D}, \tag{1.11}$$

where η_{eff} is the apparent viscosity. The variable λ represents the structural integrity of the material, taking the values $\lambda = 1$ for a fully structured state and $\lambda = 0$ for complete structural breakdown. Specific thixotropic constitutive models, such as the Houska model [37], can be incorporated within this generic framework.

Structural Kinetic Modeling

Rather than modeling microstructural details explicitly, which can span multiple hierarchical scales from individual particles to network-like aggregates, phenomenological Structural Kinetic Models (SKMs) introduce a single scalar structure parameter ($\lambda(t)$) that represents the current degree of structural organization in the material [30], [32], [38], [39], [40]. This parameter increases during rest or weak deformation ($\lambda \to 1$), reflecting the slow rebuilding of microstructural connectivity, and decreases during flow when hydrodynamic forces disrupt the existing structure ($\lambda \to 0$). The stress response of the material is then written so that its viscosity or yield stress depends on the value of this structure parameter, making the apparent material properties dependent on flow history rather than only the instantaneous shear rate. SKMs reflect the classical interpretation of thixotropy as a competition between flow-induced destructuring and thermodynamic or interaction-driven restructuring.

The evolution of the structure parameter is typically expressed through a kinetic equation balancing these two processes, without requiring assumptions about the precise structural state. In soft matter systems observable signatures of thixotropy such as viscosity bifurcation, hysteresis, and flow-induced structural changes can arise from processes occurring at different length scales depending on concentration and applied stress. SKMs are particularly useful here because they capture this evolving behaviour through a single internal variable ($\lambda(t)$), even when the microstructural mechanisms differ across regimes [31], [41], [42].

When these rheological descriptions are used in continuum flow calculations, the structure parameter becomes a field variable that is advected and locally evolved within the incompressible Navier–Stokes equations. The stress at every point in the flow depends on the instantaneous local value of the structure parameter, while the rate of structural change at that point depends on the local deformation rate. Thus, flow influences structure and structure influences flow in a coupled manner. This coupling naturally produces spatially heterogeneous responses such as shear banding, delayed yielding, and flow-history–dependent viscosity fields. Because the structure evolves more slowly than the velocity field, the material can retain memory of previous deformation, leading to hysteresis between increasing and decreasing shear sweeps and to slow recovery after flow cessation.

A general form of the kinetic or rate equation can be written as follows:

$$\frac{d\lambda(t)}{dt} = \underbrace{k_1 \, \dot{\gamma}^{\,a} \lambda(t)^{\,b}}_{\text{Breakdown}} + \underbrace{k_2 \, \dot{\gamma}^{\,c} \left(1 - \lambda(t)\right)^{d}}_{\text{Buildup}} \tag{1.12}$$

where, k_1, k_2 are breakdown and buildup coefficient respectively. Whereas, indices a, b, c, d can assume different values depending on the type of SKM used. Note that while the kinetic equation can be analytically solved for a few simpler formulations, solving more complex nonlinear SKM formulations

require numerical methods. The kinetic equation can be coupled with an Equation of State (EOS) to obtain the stress field.

$$\boldsymbol{\tau} = 2\,\eta_{\text{eff}}(\dot{\gamma}, \lambda)\,\mathbf{D}, \tag{1.13}$$

1.6 Structural Aspects: Evolution of Microstructure and Rheology with Volume Fraction

The Derjaguin–Landau–Verwey–Overbeek (DLVO) theory [43], [44] describes the net interaction potential ($U(r)$) between two colloidal particles as a superposition of electrostatic double-layer repulsion, $U_{\text{el}}(r)$, and van der Waals attraction, $U_{\text{vdW}}(r)$:

$$U(r) = U_{\text{el}}(r) + U_{\text{vdW}}(r) \tag{1.14}$$

At short separation distances, particles experience an additional steep steric or Born-type repulsion that prevents overlap. The electrostatic contribution decays exponentially with interparticle distance due to the diffuse ionic layer surrounding each particle, while the van der Waals attraction decays roughly as an inverse power law and becomes significant at near-contact distances. Depending on the balance between these contributions, two limiting classes of interaction potentials emerge: repulsive and attractive systems. The behaviour of colloidal suspensions with hard spherical particles is governed primarily by how the microstructure evolves as the particle volume fraction Φ increases [45], [46]. Fig. 1.7(a) and (b) summarize the evolution of microstructure and corresponding rheological regimes for repulsive and attractive colloids respectively, as Φ increases, based on the phase behaviour.

- **Repulsive Systems:** For $\Phi < 0.49$, the suspension is a fluid in which particles diffuse freely and the rheological response is viscous-dominated

($G'' > G'$). Between $\Phi \approx 0.49$ and 0.54, the system enters a fluid–crystal coexistence region. At $\Phi \approx 0.54$, a crystalline phase forms with a solid like behaviour arising from ordered packing rather than attractive bonding, resulting in the formation of weak rheological gel ($G' > G''$). As Φ increases further, a transition to a repulsive glass occurs at $\Phi \approx 0.58$, where particle motion becomes restricted as geometric caging intensifies. In this regime, the material exhibits solid-like behaviour ($G' > G''$) and develops a measurable yield stress. Upon approaching the maximum random packing fraction ($\Phi \approx 0.63$), the system becomes fully kinetically arrested. Φ cannot be further increased without deforming the particles. These structural features correspond to an interaction potential that is dominated by repulsion: a monotonic decay from strong short-range repulsion to zero at large separations, with no attractive minimum. Electrostatic or steric stabilization therefore prevents the formation of a microstructural gel, even though rheological solidification occurs at high Φ [47].

- **Attractive Systems:** Attractive colloids undergo a distinct sequence of microstructural transitions with increasing Φ because particles readily form clusters or flocs. For $\Phi < 0.05$, the suspension behaves as a dilute fluid, whereas for $0.05 \lesssim \Phi < 0.10$, weak clusters form but do not yet percolate. At $\Phi \approx 0.10$, these clusters connect into a space-spanning percolated network, marking the formation of a microstructural gel (also known as colloidal gel). In this state, the system becomes solid-like with $G' > G''$ and a finite yield stress. As Φ increases toward $\Phi \approx 0.30$, the gel network densifies, producing a strong gel. For $\Phi \gtrsim 0.50$, attractive colloids enter an attractive glass regime in which particles are arrested by a combination of bonding and crowding, leading to a large elastic modulus and slow structural relaxation. Approaching the

maximum packing fraction ($\Phi \approx 0.60$), the system becomes a jammed attractive glass [48], [49]. This behaviour reflects an interaction potential containing a deep primary minimum at contact. The ability of particles to populate this minimum leads to aggregation, network formation, and ultimately attractive glass formation, in contrast to the purely crowding-driven arrest seen in repulsive systems. This ability of particles to form and reform attractive contacts is the primary origin of thixotropy in attractive colloids, as the percolated network breaks down under shear and rebuilds when the shear is removed [16].

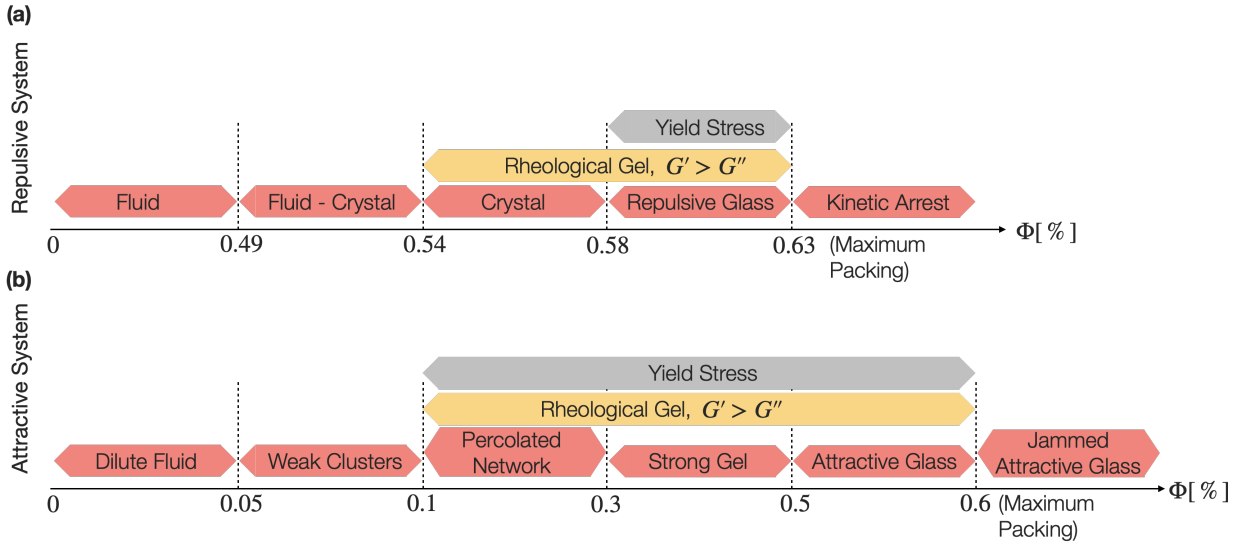

Figure 1.7: Qualitative comparison of microstructural and rheological regimes in attractive and repulsive colloidal systems as a function of particle volume fraction Φ.

1.7 Neural Networks: General Formulation

Artificial Neural Networks (ANNs) are flexible function approximators that aim to represent an unknown relationship between input and output variables [50], [51], [52]. Given an input vector $\mathbf{x}$ and a corresponding output $\mathbf{y}$, the

goal is to approximate the mapping

$$\mathbf{y} = \mathcal{F}(\mathbf{x}), \tag{1.15}$$

using a parameterized model $\hat{\mathbf{y}} = \mathcal{F}_\theta(\mathbf{x})$, where θ denotes the set of trainable model parameters (weights and biases). The objective of training is to adjust θ so that $\mathcal{F}_\theta$ reproduces the underlying input-output relationship with sufficient accuracy and generalization capability.

A feed-forward neural network consists of layers of interconnected computational units, or neurons. For an input vector $\mathbf{x} \in \mathbb{R}^d$, the transformation performed by a single hidden layer with n neurons is given by

$$\mathbf{h} = \sigma(\mathbf{W}\mathbf{x} + \mathbf{b}), \tag{1.16}$$

where $\mathbf{W} \in \mathbb{R}^{n\times d}$ and $\mathbf{b} \in \mathbb{R}^n$ are the layer weight matrix and bias vector respectively, and $\sigma(\cdot)$ is a nonlinear activation function (e.g., tanh [53], ReLU [54], sigmoid [52]). $\mathbf{h} \in \mathbb{R}^n$ is the hidden-layer activation vector, representing the nonlinear feature transformation produced by the layer. Stacking multiple layers produces a composite nonlinear mapping:

$$\mathcal{F}_\theta(\mathbf{x}) = \mathbf{W}^{(L)}\sigma\left(\mathbf{W}^{(L-1)}\sigma\left(\cdots\sigma(\mathbf{W}^{(1)}\mathbf{x} + \mathbf{b}^{(1)})\cdots\right) + \mathbf{b}^{(L-1)}\right) + \mathbf{b}^{(L)}, \tag{1.17}$$

where L is the total number of layers. The nonlinear activation functions are essential; without them, the network reduces to a linear transformation regardless of depth. A typical neural network architecture is illustrated in Fig. 1.8.

The parameters $\theta = \{\mathbf{W}^{(l)}, \mathbf{b}^{(l)}\}_{l=1}^{L}$ are optimized by minimizing a loss function $\mathcal{L}$ that measures the discrepancy between predicted and observed outputs. For supervised regression problems, a common choice is the mean

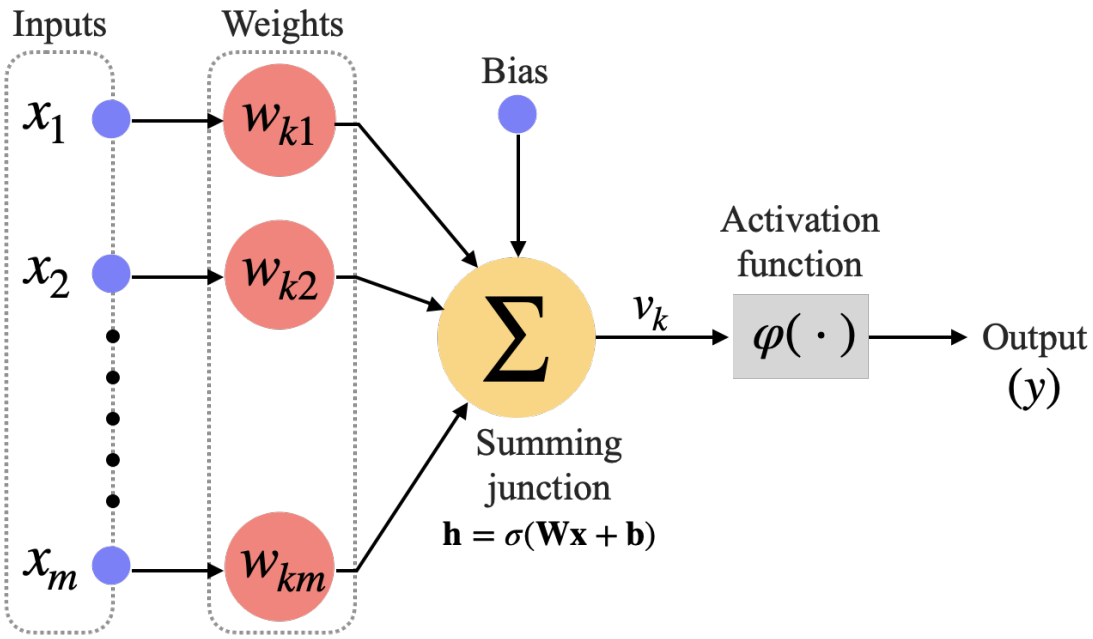

Figure 1.8: Schematic illustrating a typical neural network architecture.

squared error (MSE):

$$\mathcal{L}_{\text{data}} = \frac{1}{N} \sum_{i=1}^{N} \|\hat{\mathbf{y}}_i - \mathbf{y}_i\|^2 . \tag{1.18}$$

Parameter updates are typically performed using gradient-based optimization algorithms such as stochastic gradient descent or adaptive methods (e.g., Adam), with gradients computed efficiently using backpropagation.

Neural networks are universal function approximators, meaning that given sufficient capacity, they can approximate any continuous function on a compact domain. This makes them particularly powerful for representing complex, nonlinear, or high-dimensional relationships, such as those encountered in the rheological response of soft materials [55], [56].

CHAPTER 2

Materials and Methods

2.1 Materials

Laponite suspensions were used as model Thixo-Elasto-Viscoplastic (TEVP) fluids in Papers I [57] and III [58]. Laponite RD powder (Conservation Resources Ltd., UK) was gradually dispersed into deionized water while mixing vigorously with a high-shear paddle mixer (Mixer Flex MXE1602, Ahlsell, Sweden) at 2000 rpm for 30 min to prevent agglomeration and ensure complete exfoliation of the synthetic hectorite nanoplatelets. The resulting suspension was allowed to age undisturbed for 72 h to allow the colloidal microstructure to develop and reach a reproducible initial state prior to testing.

Carbopol was employed as representative yield-stress materials in Papers I [57], whereas Carbopol–PEO blends were used as Elasto-Viscoplastic (EVP) 3D printing inks in Paper IV [59]. Carbopol 980 NF (Lubrizol, USA) was dispersed in deionized water and mixed using a high-torque overhead stirrer

(Heidolph Hei Torque Ultimate 400, Heidolph Elektro GmbH, Germany) at 1200 rpm for 30 min. The acidic dispersion was then neutralized by dropwise adding 18 wt% aqueous NaOH solution [60], leading to polymer chain expansion via electrostatic repulsion among ionized carboxylate groups. The neutralized gel was further mixed for 1 h at 2000 rpm to ensure uniform network formation. For Carbopol–PEO blends, polyethylene oxide (Sigma-Aldrich, USA; $M_W = 4 \times 10^6$ Da) was dissolved separately in deionized water and fully hydrated before being combined with the Carbopol gel. The two components were mixed for 30 min to obtain blends with total polymer concentrations in the range of 0.05–0.125 wt%, enabling systematic tuning of elasticity, yield stress, and post-extrusion filament stability.

Due to its complex bio-rheology, commercial yogurt was used as a TEVP reference material in Papers I [57] and II [61]. Three varieties— Naturell (N), Vanilj (V), and Långfil (L) (Arla Foods, Viby, Denmark), were selected to represent differences in microstructure, fat content, and fermentation culture. Samples were stored at 2 °C in sealed containers and were used well within their stated shelf life to prevent changes in rheology due to continuing biochemical activity. Prior to testing, samples were allowed to equilibrate to room temperature for approximately 30 min and were gently inverted a few times to ensure homogeneity without inducing high shear that would artificially alter their initial structural state.

Finally, human saliva was collected and used to study viscoelastic and thixotropic responses in Paper V [62]. Saliva was obtained from healthy non-smoking volunteers following standard collection guidelines. Unstimulated saliva was collected by passive drooling into sterile polypropylene tubes, while stimulated saliva was collected after chewing on flavorless paraffin wax. Samples were immediately stored on ice and measured within a short time window to minimize degradation. No centrifugation or filtration was performed, so that the naturally occurring mucin networks remained intact.

Across all materials, the preparation and handling procedures were designed to avoid unintended pre-shear and to establish a reproducible and well-defined initial structural state prior to characterization. All experiments were conducted at controlled temperature conditions, and repeated measurements were performed to ensure consistency and reliability.

2.2 Rheological Characterization

Rheological measurements were performed using a rotational rheometer (Anton Paar MCR 702e Space, Graz, Austria). For yield stress fluids including Laponite suspensions, yogurt, Carbopol gels, and Carbopol-PEO blends, a profiled bob and cup geometry (CC27/P6) was used to minimize wall slip effects. The bob diameter was 27 mm and the inner diameter of the cup was 29 mm. All measurements were performed in single motor-transducer configuration. Temperature was controlled at 23°C using a C-ETD200/XL environmental cell. Samples were carefully loaded to avoid unintended pre-shear and were allowed to equilibrate in the geometry prior to testing. In contrast to the systems above, saliva was measured using parallel plate geometry (50 mm diameter) with a 1 mm gap, due to its low viscosity and high surface tension. A solvent trap was employed to minimize evaporation. The same temperature control conditions were applied as for the bob and cup measurements.

Flow curves were measured in controlled rate mode by sweeping the shear rate typically from a high to low value, holding each step long enough to reach a quasi-steady response. Time-dependent structural evolution was examined using multi-interval step-change tests (MITT), in which the sample was subjected to a sequence of constant shear rate intervals spanning values below and above the apparent yield stress. The transient stress responses provided information on thixotropic breakdown and recovery, and were used where applicable for neural network training and structural kinetic model parameter extrac-

tion. Thixotropy was measured using shear rate up/down ramps with constant time step size. The area between the ascending and descending branches of the resulting hysteresis loop was taken as a measure of thixotropy. Oscillatory strain sweep tests were performed at an angular frequency of 6 rad/s to determine the linear viscoelastic regime. Frequency sweeps at strain amplitudes within the linear viscoelastic regime were conducted when additional relaxation spectrum information was required. Yield stress was evaluated using both stress-controlled steady-shear and creep tests. In stress ramps, the transition from elastic to plastic deformation was identified from changes in the slope of the viscosity function. In creep experiments, the evolution of the apparent viscosity under constant applied stress allowed distinction between sub-yield (recovery-dominated), post-yield (breakdown-dominated), and near-yield competing regimes, providing estimates of characteristic yielding dynamics of the material.

2.3 Pipe Flow Experiments

A pilot-scale pipe flow facility was constructed in collaboration with Tetra Pak Processing Systems (Lund, Sweden) to enable controlled flow measurements in straight tubes of varying diameters, as illustrated in Fig. 2.1. The setup consisted of a 200 L feed tank connected to a rotary positive-displacement screw pump (Knoll Maschinenbau GmbH, MX30-S-50/20, maximum operating frequency 115 Hz). The pump discharged into one of five interchangeable stainless-steel pipes, each 3400 mm in length, with internal diameters ranging from 14 mm to 51 mm. Selection of the desired test pipe was achieved using a set of ball valves located upstream and downstream of the test section, allowing rapid switching between pipe diameters without draining the system.

The volumetric flow rate was measured downstream of the tank using an inline flowmeter (Endress & Hauser, Basel-Country, Switzerland). Fluid tem-

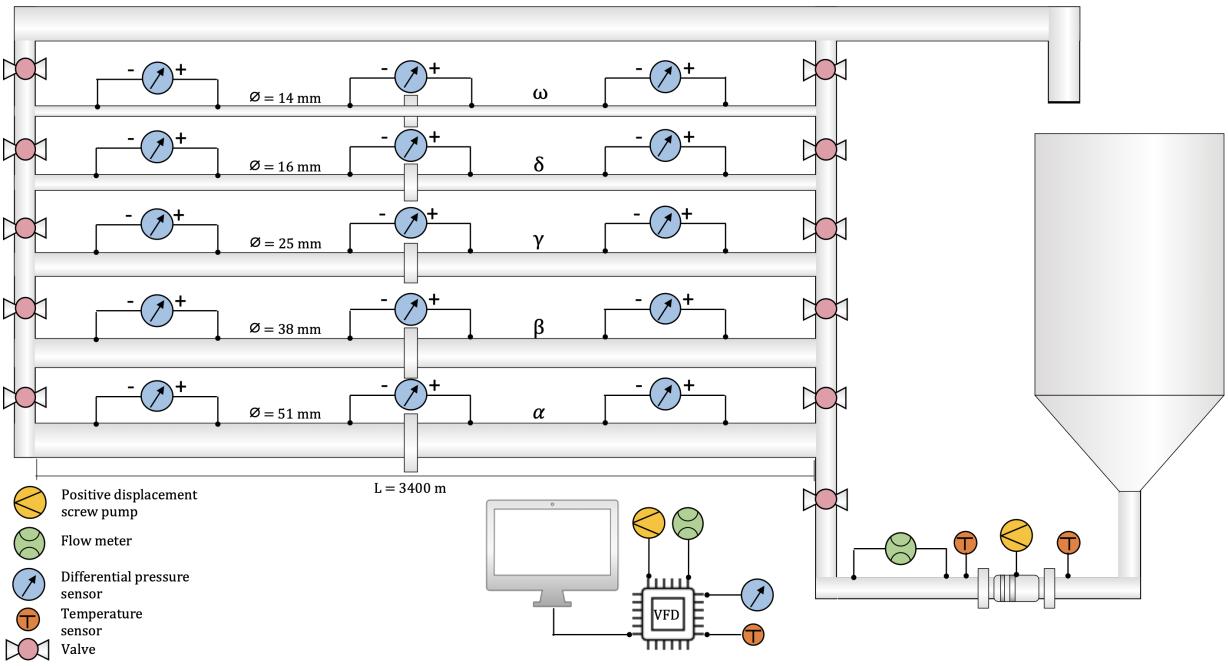

Figure 2.1: Illustration of the pilot-scale pipe rig used for pressure drop measurements.[58]

perature was monitored continuously using two thermocouples positioned immediately before and after the pump to ensure stable thermal conditions. The pressure drop along the test pipes was recorded using three metal-membrane pressure transducers (Endress & Hauser), mounted 200 mm downstream of the pipe inlet with 600 mm spacing between successive sensors. The transducers provided pressure measurements with a precision of 0.05%. Prior to each experimental run, the pressure sensors were zeroed with the pipe empty, and the measurement system was calibrated using water (viscosity = 1.0 mPa·s) at 22.7 °C, and a relative humidity of 44.5%. Pump speed, and thus flow rate, was controlled through a variable-frequency drive (Nordborg, Denmark). Pressure, temperature, and flowrate data were logged at 1 Hz using a LabView 2018 data acquisition system (National Instruments, USA).

For each experiment, Laponite suspensions were prepared in 60 L batches, transferred into the feed tank, and allowed to relax so that any shear history

introduced during handling could dissipate. The appropriate pipe was then filled at a low flow rate of 300 L/h to avoid disrupting the microstructure. Once the pipe was filled, the system was left to equilibrate for approximately 30 minutes under quiescent conditions. Flow measurements were then performed in recirculating mode, wherein the fluid exiting the pipe outlet returned to the feed tank and was continuously pumped through the same test section. Each circulation experiment was conducted for 300 s to ensure stable and reproducible flow measurements.

2.4 3D Printing Setup and Data Analysis

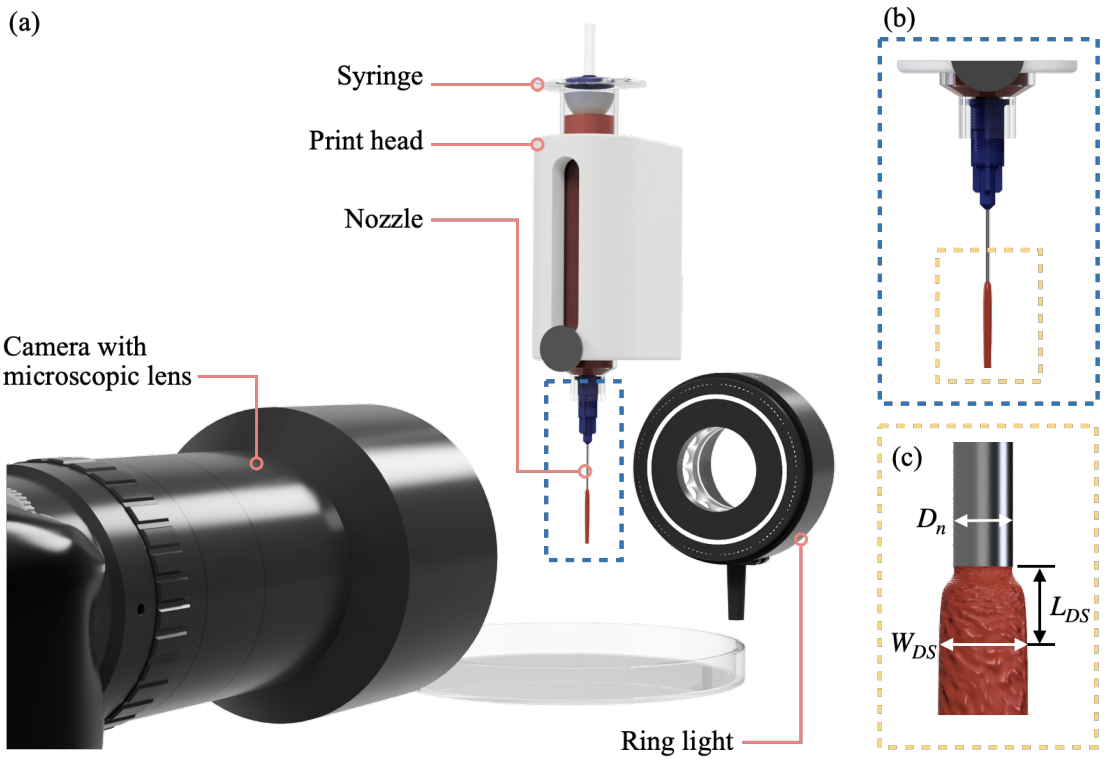

Figure 2.2: Illustration of the 3D printing and visualization setup.[59]

3D printing experiments were performed using a BIO-X bioprinter (Cellink AB, Gothenburg, Sweden) equipped with a pneumatic dispensing system. The

samples were loaded into 3 mL syringes fitted with 22G blunt needles (inner diameter $D_n = 0.41$ mm). A fiber-optic ring illumination system (Dolan-Jenner, Edmund Optics, USA) was positioned behind the printhead against a non-reflective black background to provide uniform lighting for imaging. High-speed video recordings were captured at 120 frames/s using a Canon EOS 90D camera (Canon Inc., Tokyo, Japan) equipped with a microscope lens system (LMscope, Austria). The setup is illustrated in Fig. 2.2.

To prevent air entrapment, the blends were slowly introduced into the syringe, and any remaining bubbles were removed using a vortex mixer. Extrusion was performed at applied pneumatic pressures of 100, 150, and 200 kPa. Once steady filament formation was observed, video frames were extracted and analyzed. Image processing, including color normalization, was carried out using custom MATLAB routines to determine the die-swell width (W_{DS}) and the corresponding swell position (L_{DS}). Each experiment was repeated three times, and mean values of W_{DS} were extracted.

The same setup was used for 3D-printing tests. The needle height was adjusted to D_n to maintain a stable deposition gap. Several print speeds were examined, and a velocity of $V_P = 50$ mm/s was selected as it produced continuous, stable filaments while minimizing spreading upon deposition. Printed lines were imaged, and the final deposited width (W_P) was determined at three positions along the filament and averaged.

2.5 Rheo-SAXS

Rheology-coupled small-angle X-ray scattering (Rheo-SAXS) measurements were carried out at the CoSAXS beamline at the MAX IV Laboratory (Lund, Sweden). The X-ray energy was set to 15 keV, and a sample-to-detector distance of 14.8 m (EIGERX 4M detector) provided access to a scattering vector range of $q \in (10^{-3}, 8 \times 10^{-1})$ Å^{-1}.

Rheological control during the scattering experiments was achieved with an Anton Paar MCR 702 Multidrive rheometer (Anton Paar, Austria) equipped with a polycarbonate concentric cylinder (CC) measuring geometry (inner cylinder radius 24.5 mm, outer radius 25 mm). To study structural relaxation following strong deformation, each experiment consisted of two steps: (i) an imposed shear at $\dot{\gamma} = 10^3\,\mathrm{s}^{-1}$ for 30 s to disrupt the microstructure, and (ii) a prolonged relaxation phase at $\dot{\gamma} = 10^{-4}\,\mathrm{s}^{-1}$ lasting 3000 s. Scattering data was collected continuously during both intervals with an exposure time of 0.1 s, sampling the scattering response in the radial direction of the CC geometry (1-3 plane) [63].

Data integration and processing was carried out using a Python/Jupyter Notebook workflow adapted from the CoSAXS beamline analysis tools. Each two-dimensional detector frame was normalized for transmission to correct for variations in beam intensity and exposure time on a per-frame basis. The transmission-corrected patterns were then azimuthally integrated to yield one-dimensional $I(q)$ curves. A separate dataset acquired with the polycarbonate concentric cylinder measuring geometry filled with water was processed in the same way and subsequently subtracted to remove background scattering. The corrected scattering intensity used in the analysis is given by:

$$I(q) = I_{\mathrm{raw}}^{\mathrm{norm}}(q) - I_{b}^{\mathrm{norm}}(q), \tag{2.1}$$

where $I_{\mathrm{raw}}^{\mathrm{norm}}(q)$ and $I_{b}^{\mathrm{norm}}(q)$ denote the normalized, radially integrated intensities of the sample and background, respectively.

The normalization factor applied to each frame was computed as:

$$\mathrm{norm} = \frac{I_t - I_{\mathrm{dark},t}}{I_0 - I_{\mathrm{dark},0}} \times \frac{I_{\mathrm{empty},0} - I_{\mathrm{dark},0}}{I_{\mathrm{empty},t} - I_{\mathrm{dark},t}} \times \mathrm{dt}, \tag{2.2}$$

where I_0 and I_t are the incident and transmitted intensities recorded during the measurements, $I_{\mathrm{dark},0}$ and $I_{\mathrm{dark},t}$ are the corresponding dark signals, $I_{\mathrm{empty},0}$

and $I_{\text{empty},t}$ refer to measurements obtained with the empty polycarbonate geometry, and dt is the exposure time. The resulting $I(q)$ profiles were used to monitor microstructural evolution during shear cessation and subsequent structural recovery. The effective radius of gyration (R_g) of the material structures was obtained by fitting a quadratic equation to the Guinier plot ($\ln(I)$ vs. q^2).

$$\ln(I) = -\frac{R_g^2}{3} \cdot q^2 + \ln(I_0) \tag{2.3}$$

2.6 Surface Tension

Surface tension was measured to quantify the interfacial properties of the materials used in this study and to support the analysis of filament formation, die swell, and spreading during extrusion and printing. Measurements were performed using a pendant drop tensiometer (Attension Theta, Biolin Scientific), where a droplet was formed at the tip of a needle (diameter = 0.718 mm) and imaged under backlighting. The droplet profile was fitted to the Young-Laplace equation, which relates the pressure difference across a curved interface to the surface tension as $\Delta P = \gamma \left(\frac{1}{R_1} + \frac{1}{R_2}\right)$, where R_1 and R_2 are the principal radii of curvature of the interface at the point where the pressure difference is evaluated. For a pendant drop under gravity, the pressure difference varies with depth according to $\Delta P(z) = \Delta P_0 + \rho g z$, where ΔP_0 is the pressure at the apex, ρ is the liquid density, and g is the gravitational acceleration. By fitting the measured droplet silhouette to the corresponding Young-Laplace shape, the equilibrium surface tension γ was determined. Each sample was measured in triplicate to ensure reproducibility, and the reported values represent the average of these replicates.

2.7 Density Measurements

Sample density was quantified using a gas pycnometry system (Ultrapyc 5000, Anton Paar, Graz, Austria) pressurized with nitrogen at a controlled temperature of 20°C. Samples were gently introduced into the measurement chamber to minimize entrapment of air bubbles. For each material, five consecutive measurements were performed, with the resulting density values showing a variation of less than 0.1%.

2.8 Morphological Characterization

The microstructure of the yogurt samples was examined using an environmental scanning electron microscope (ESEM; Philips XL–30, Amsterdam, Netherlands). To capture the internal structure at specific stages of the experiments, small portions of the material were gently removed from the rheometer cup using a spatula. The microstructure was immobilized by rapidly plunging the collected sample into liquid nitrogen, after which the material was freeze-dried for 72 h to remove water while preserving network architecture. After freeze-drying, a fragment of the sample was mounted to an aluminum SEM stub using carbon adhesive tape. To prevent charging during imaging and to improve surface conductivity, the sample was coated with a thin (5 nm) gold layer using a vacuum sputter coater. Images were acquired under high-vacuum mode at suitable beam voltages chosen to balance resolution and beam-induced damage. Post-processing and quantitative image analysis were performed using the Fiji image analysis suite. The raw micrographs were converted to binary images and then processed using the 'skeletonize' algorithm, which reduces the structure to a network map. This skeleton mapping enabled qualitative comparison of structural connectivity.

Microstructural imaging of Carbopol, Laponite and Yogurt samples was car-

ried out using a Nikon A1 Ti-E confocal laser scanning microscope (CLSM, Nikon, Tokyo, Japan). Highly thixotropic formulations were selected as representative samples for visualization. To fluorescently label the materials, a Rhodamine 6G solution (10 µg/mL in acetone; Merck, Darmstadt, Germany) was prepared and applied to glass slides. After the solvent had fully evaporated, small quantities of each sample were placed on the stained region and covered with a cover slip. Fluorescence excitation was performed using a 488 nm Ar/Kr laser line. Images were acquired at a resolution of 1024 × 1024 pixels, corresponding to 0.8 µm/pixel for the yogurt and Laponite samples, and 0.4 µm/pixel for the Carbopol sample.

2.9 Millifluidic Channel Geometry and Experimental Setup

The flow measurements were carried out in a rectangular millifluidic channel with an internal cross-section of 1.00 mm in height and 3.25 mm in width, see the schematic overview in Fig. 2.3.. The channel was constructed as a three-layer assembly, where the central layer consisted of a 1 mm stainless-steel plate in which the channel geometry was machined. This metal layer was sandwiched between two transparent PMMA plates, each 3 mm thick, providing optical access for imaging. The complete structure was clamped between two rigid aluminum plates to ensure mechanical stability and prevent leakage during operation.

Fluid was supplied to the channel using a syringe pump connected to the inlet via flexible tubing. The outlet tubing discharged into an open reservoir at ambient pressure. The imposed volumetric flow rates ranged from 0.4 to 5.0 mL/min, corresponding to laminar flow regimes. The velocity measurements were performed at a streamwise location approximately 65 mm downstream from the inlet. Preliminary scans along the channel length were used to con-

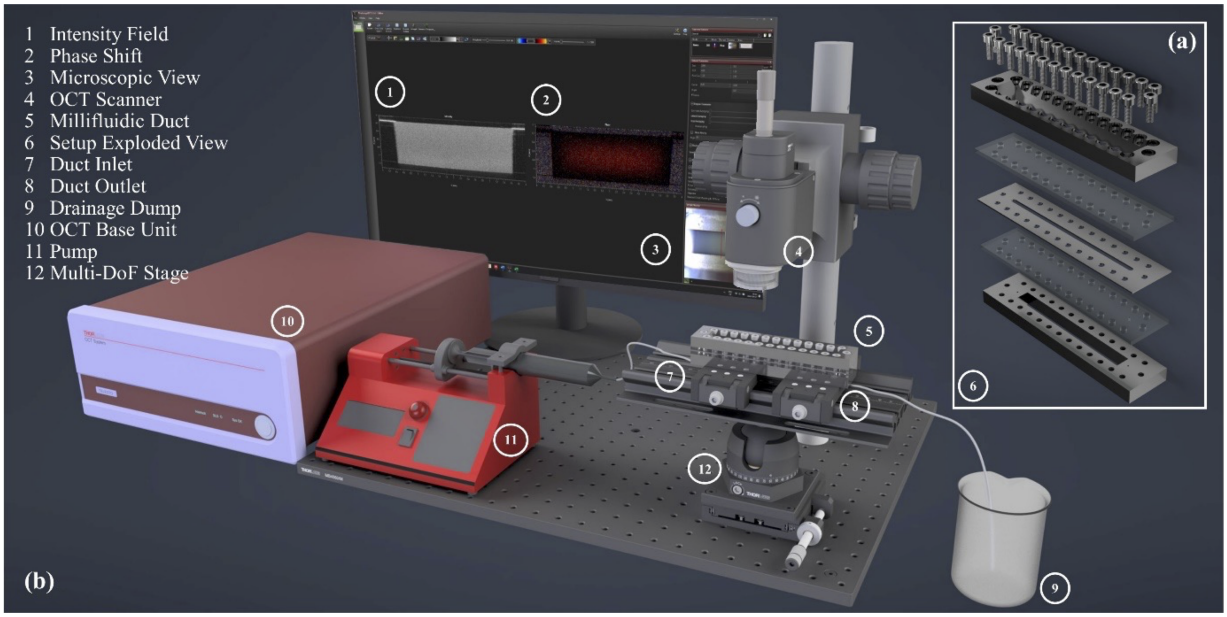

Figure 2.3: Illustration of the millifluidic geometry and the OCT setup.[57]

firm that the flow was fully developed at this position, meaning that the velocity profile no longer significantly varied in the streamwise direction. Velocity profiles were extracted normal to the upper wall of the channel, focusing on the near-wall region. This is the region in which structural yielding, wall slip, and plug formation effects are most pronounced.

2.10 Doppler Optical Coherence Tomography (D-OCT)

The internal velocity field was measured using spectral-domain Doppler optical coherence tomography (D-OCT, Thorlabs, Newton, NJ, USA), which enables depth-resolved velocity imaging in opaque as well as transparent weakly scattering fluids. The method relies on low-coherence interferometry, in which the light from a broadband near-infrared source is split into a reference beam and a sample beam directed into the flowing fluid. Backscattered light from within the fluid interferes with the reference light, producing an interference pattern from which depth-resolved intensity information is obtained. Velocity

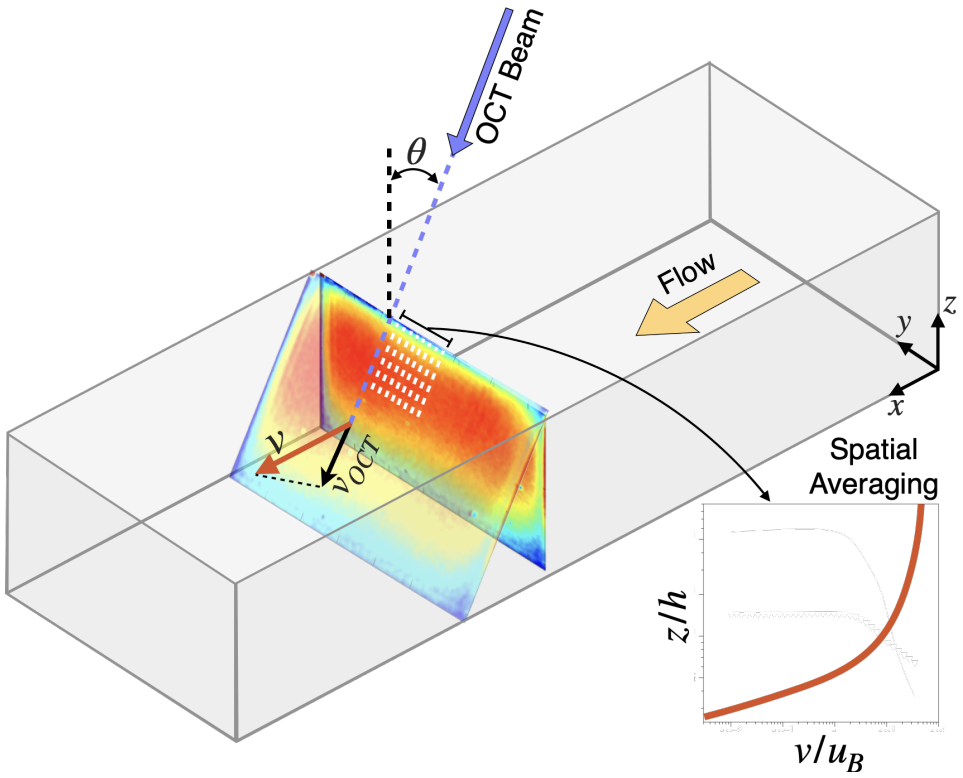

Figure 2.4: Orientation of the flow setup with respect to the OCT beam direction. Streamwise velocity is obtained as a function of the Doppler frequency shift $\Delta\omega$.[57]

information is extracted from the Doppler frequency shift of the backscattered signal (Fig. 2.4). As fluid microstructures move relative to the incident beam, they induce a shift in the optical phase proportional to the velocity component along the beam direction. Since the OCT beam was introduced at a small fixed inclination angle ($\theta = 7°$) relative to the primary flow direction, the measured velocity component was converted to the axial velocity using the known projection angle, according to Eq.2.4 - 2.5.

$$\Delta\phi = \Delta\omega\Delta t = \frac{4\pi v}{\lambda_0 f} \tag{2.4}$$

$$v = \frac{\lambda_0 f \Delta\phi}{4\pi cos\theta} \tag{2.5}$$

where, f is the OCT acquisition frequency, $\Delta\omega$ is the Doppler angular frequency shift, Δt is the time interval between successive scans, $\Delta\phi$ is the corresponding phase shift, λ_0 is the central wavelength of the OCT source, and θ is the inclination angle between the OCT beam and the flow direction.

For each experimental condition, a sequence of approximately 500 consecutive OCT frames was recorded at high acquisition rates. These frames were then ensemble-averaged to reduce noise and improve signal stability. To further minimize spatial fluctuations due to surface imperfections or local scattering variations, velocity profiles were additionally averaged across several adjacent scan lines in the spanwise direction. This procedure provided high-resolution velocity profiles with sufficient spatial precision to resolve the near-wall shear region and to identify features such as wall slip, shear-induced fluidization, and the presence of unyielded plug-like regions.

CHAPTER 3

Summary of results

This chapter summarises the main scientific contributions of the thesis and highlights how rheology, flow measurements, computational fluid dynamics, and data-driven modeling are integrated to understand and predict the behaviour of soft matter across diverse flow geometries. It is organised into five parts: pressure-driven flow of TEVP fluids in rectangular millifluidic channels (Paper I), neural network based rheological modeling of TEVP fluids (Paper II), transient pipe flow of thixotropic yield stress fluids in circular tubes (Paper III), extrusion and 3D printing of elasto-viscoplastic fluids (Paper IV), and the rheology of human saliva with implications for xerostomia / dry mouth (Paper V).

3.1 Soft Matter Flow in Rectangular Millifluidic Channels

To interpret the flow behavior of thixo-elasto-viscoplastic (TEVP) fluids in confined millifluidic geometries, it is essential to connect their rheological response to the flow fields that develop under pressure-driven conditions. Bulk rheology provides the key material parameters—viscoelasticity, yield stress, and thixotropy—that govern structural evolution under the spatially varying shear fields present in channel flow. Doppler Optical Coherence Tomography (D-OCT) is used to obtain depth-resolved axial velocity profiles, enabling identification of shear localization, wall slip, and unyielded plug regions. Near-wall velocity gradients provide local shear rates, which are converted to wall shear stresses through an ex situ rheological protocol, allowing direct comparison between the in-flow stress response and rheometer-measured behavior. Fluids with a pronounced yield stress and limited structural breakdown exhibit a large unyielded plug core, often extending close to the wall. In contrast, materials with strong thixotropic behaviour undergo additional structure breakdown under flow, leading to reduced plug thickness and velocity profiles that approach the Newtonian Boussinesq limit. By integrating rheological material functions with the measured flow fields, dimensionless groups and scaling laws can be constructed that collapse diverse datasets onto universal curves. These relations reveal how intrinsic material properties dictate wall shear stress, slip behavior, and the evolution of the velocity profile, providing a unified framework for comparing TEVP flows across materials and geometries.

Rheological Material Response Functions

Three differrent TEVP materials (three variants/concentrations each) were chosen (Table.3.1). Viscoelastic, viscoplastic and thixotropic material functions are presented in Fig. 3.1. All the samples exhibit shear thinning be-

Table 3.1: Type/Concentration of the TEVP fluids and their designations used in this study.

Sample	Type / Conc. [wt %]	Designation
Yogurt	Naturell	Y1
	Vanilj	Y2
	Långfil	Y3
Carbopol	0.1	C1
	0.2	C2
	0.6	C3
Laponite	1	L1
	2	L2
	3	L3

haviour, but the extent of time-dependent structural breakdown and recovery varies markedly across materials and concentrations (Fig. 3.1(a–c)). For yogurt, the hysteresis loop area (A_{hys}) increases from Y1 to Y3, indicating progressively greater thixotropy. Carbopol gels show the weakest time-dependent effects: C1 and C2 have negligible thixotropy, while C3 displays only a modest increase in A_{hys}. Laponite suspensions exhibit the strongest thixotropy overall, with A_{hys} increasing sharply from L1 to L3, reflecting the significant breakdown of the platelet network and its slow recovery upon shear reduction.

Oscillatory measurements corroborate these structural trends (Fig. 3.1(d–f)). All materials exhibit gel-like behavior with $G' > G''$ in the linear viscoelastic region, and G' increases from samples 1 to 3 within each material family, reflecting progressively stronger elasticity. Yogurt has the lowest moduli, Carbopol is substantially stiffer, and Laponite, especially L3, shows the strongest elastic response. The weak stress overshoot (WSO) during the transition to LAOS follows the same hierarchy: yogurt shows only gradual softening without any overshoot, whereas Carbopol and Laponite display increasingly pronounced overshoots from sample 1 to 3, consistent with more interconnected

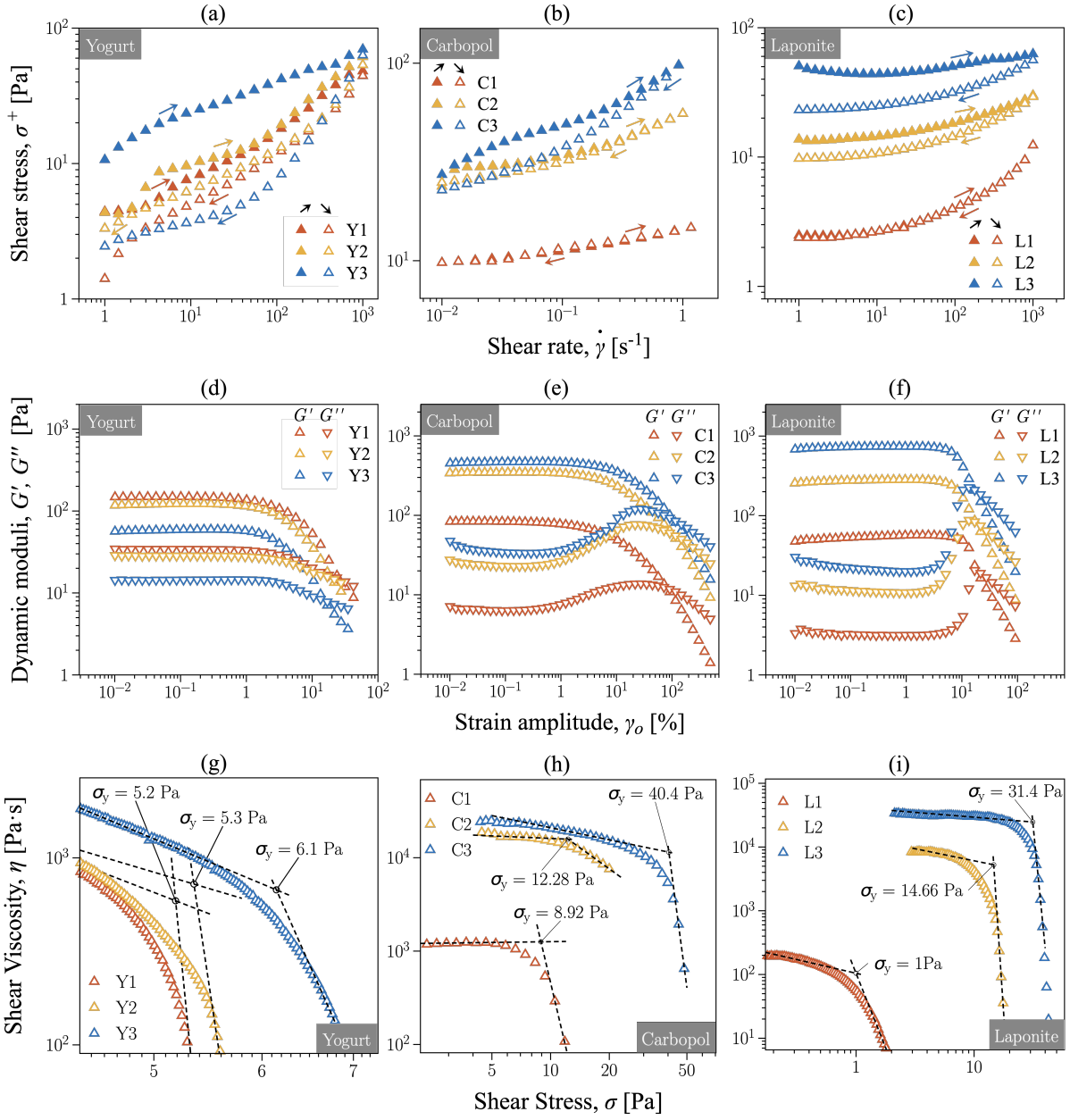

Figure 3.1: Rheological functions used to measure (a) thixotropy, (b) viscoelasticity, and (c) yield stress of the chosen TEVP fluid types/concentrations.

networks that resist deformation before yielding.

The static yield stress (σ_y) obtained from stress-controlled tests is shown in Fig. 3.1(g-i). Within each material class, σ_y increases consistently from sample 1 to 3. Yogurt exhibits low yield stresses, Carbopol shows moderate values in C1 and C2 and a substantially higher value in C3, while Laponite spans a wide range from very weakly yielding in L1 to much higher values in L3.

The combination of high yield stress, large WSO, and strong thixotropy in L2 and L3 reflects the formation of a strong, but shear sensitive platelet network. In contrast, C1 and C2 display moderate σ_y together with low thixotropy, indicating that their microgel network yields easily when sheared but recovers quickly, predominantly in a reversible, elastic manner. Whereas C3, with its much higher σ_y and WSO, exhibits a more robust and less easily deformed structure. The yogurt samples, which have the lowest yield stress but strong thixotropic effects, form comparatively weak structures that yield readily and undergo substantial time dependent structural rearrangements, leading to incomplete or slow recovery of their original microstructure.

Flow Field

The velocity fields measured by Doppler OCT reveal a spectrum of flow behaviors that can be correlated directly with the linear viscoelastic moduli, yield stress, thixotropic loop area, and weak strain overshoot identified in the rheological characterization (Fig. 3.1). These range from nearly Newtonian-like profiles to strongly plug-dominated flow, depending on the strength and shear sensitivity of the microstructure.

Samples C1 and L1 (Fig. 3.2(d,g)) show velocity profiles that closely follow the analytical Boussinesq solution. Their relatively high $\tan\delta = G''/G'$ indicates that viscous dissipation dominates over elastic contributions, and their low yield stress and thixotropy result in minimal structural rearrangements

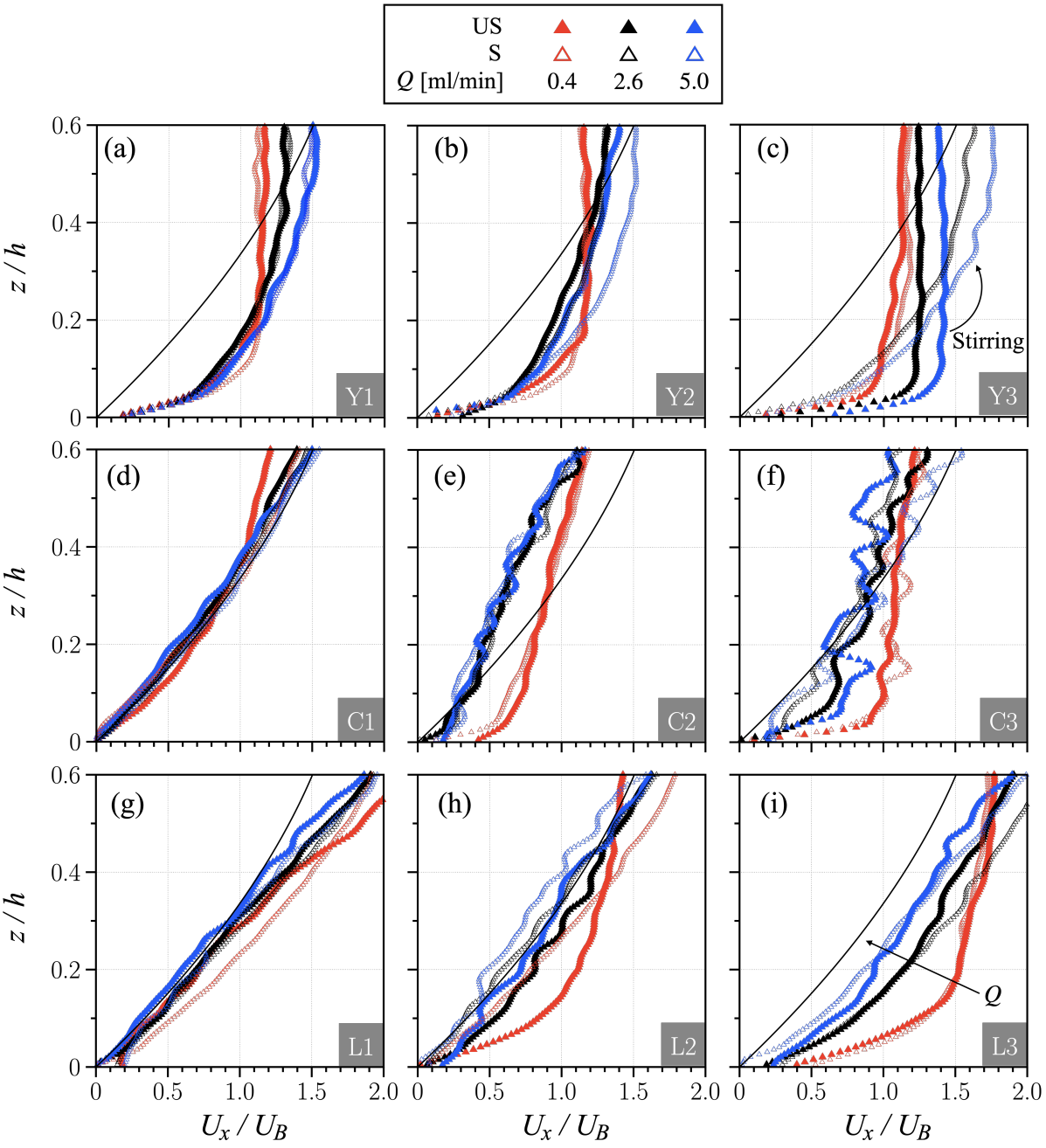

Figure 3.2: Velocity profiles of stirred and unstirred (a-c) yogurt, (d-f) Carbopol, and (g-i) laponite samples at three different flow rates.[57]

under deformation. Consequently, the velocity transitions smoothly from center to wall without forming a pronounced plug.

In contrast, samples C2, C3, L2, and L3 (Fig. 3.2(e,f,h,i)) exhibit steeper near-wall gradients and a finite plug. Their lower $\tan\delta$ reflects stronger solid-like behavior, and the microstructural jamming associated with weak strain overshoot produces sharper transitions at the yield boundary. Overshoots are smaller in C2 and C3 than in L2 and L3, consistent with the reduced shear banding observed. The strong elasticity, high yield stress, and rapid structural recovery of Laponite cause only minor differences between the stirred and unstirred profiles.

Yogurt samples Y1-Y3 (Fig. 3.2(a,b,c)) display broad plug regions and diffuse shear-localized zones near the wall. Their higher $\tan\delta$ compared to Carbopol and Laponite indicates a greater viscous contribution, and the absence of WSO suggests continuous yielding through gradual breakdown rather than sudden jamming. Plug size increases from Y1 to Y3 in accordance with their increasing yield stress and thixotropic loop area, indicating ongoing structural breakdown and slow recovery under flow. Stirring reduces plug thickness, most notably for Y3, which exhibits the strongest thixotropy and the slowest recovery.

Overall, Newtonian-like behavior appears in samples with low G', low yield stress and thixotropy, and no WSO (C1, L1), while samples with higher G', and considerable overshoot, yield stress and thixotropy, develop sharper near-wall gradients (C2, C3, L2, L3). Systems with large $\tan\delta$, moderate yield stress and high thixotropy form wide plug regions (Y1-Y3).

Scaling Laws

To compare the near-wall flow behavior across materials that differ in yield stress, thixotropy, and viscoelastic behaviour, a dimensional analysis was carried out and four non-dimensional groups were constructed following a bottom-

up Buckingham–Pi approach. The resulting groups combine (i) material-level parameters such as the yield stress σ_y, the corrected hysteresis loop area A^*, and the near-wall viscosity $\eta(\dot{\gamma}_w)$, with (ii) flow-level quantities such as the local near-wall shear rate $\dot{\gamma}_w$ and the slip velocity u_s. The four selected dimensionless parameters are

$$\Pi_1 = \frac{\dot{\gamma}_w \, \sigma_y^3}{A^{*\,2} \, \eta(\dot{\gamma}_w)}, \tag{3.1}$$

$$\Pi_2 = \frac{\eta(\dot{\gamma}_w) \, A^*}{\sigma_y^2}, \tag{3.2}$$

$$\Pi_3 = \frac{\rho \, u_s^2}{\tau_w}, \tag{3.3}$$

$$\Pi_4 = \frac{A^* \, \ell^2}{\eta(\dot{\gamma}_w) \, u_s^2}, \tag{3.4}$$

where τ_w is the wall shear stress and $\ell = \sqrt{\nu/\dot{\gamma}_w}$ is the characteristic near-wall length scale associated with the local shear rate. The quantity A^* represents a normalized hysteresis loop area,

$$A^* = A_{\mathrm{hys}} \left(\frac{\tau \dot{\gamma}}{A_{up}} \right), \tag{3.5}$$

which provides a relative measure of shear-induced structural breakdown, independent of absolute stress scale. Larger A^* corresponds to materials whose internal network is more strongly disrupted under flow.

Fig. 3.3(a) shows that Π_1 collapses onto a single power-law relationship when plotted against Π_2 for all samples, spanning more than three decades in Π_2 and over five decades in Π_1. Because Π_1 and Π_2 are constructed only from rheological quantities and the near-wall shear rate, this collapse demonstrates that once the shear rate dependence of viscosity is known, the wall shear stress τ_w can be determined directly from bulk rheological measurements without re-

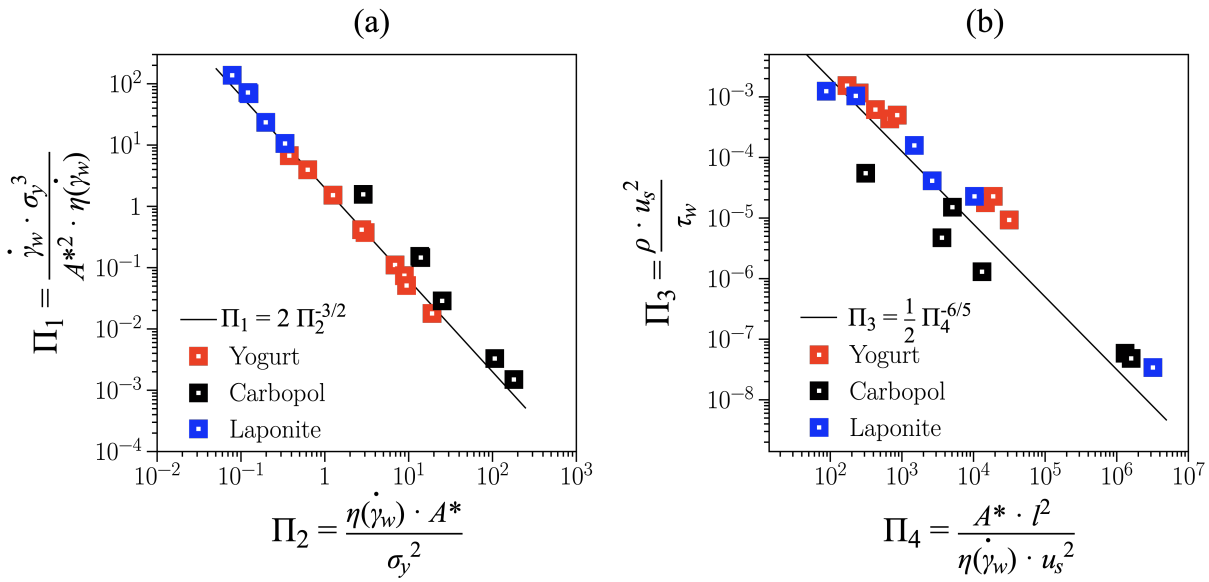

Figure 3.3: Scaling laws based on four dimensionless quantities that can be used to determine the wall shear stress (τ_w) and the slip velocity (u_s) in the near wall region of a rectangular duct.[57]

quiring high-resolution flow-field data. In practical terms, τ_w may be obtained from $\tau_w = \eta(\dot{\gamma}_w)\,\dot{\gamma}_w$ once the Π_1–Π_2 scaling is used.

With τ_w determined, the slip velocity u_s becomes the remaining unknown in the flow description and is obtained using the scaling between Π_3 and Π_4 (Fig. 3.3(b))). This relation spans nearly six orders of magnitude in both Π_3 and Π_4. Notably, Π_3 resembles a Reynolds number like ratio for the near-wall region, indicating that slip is controlled by the inertial to viscous balance at the interface.

These scaling laws hold across a wide range of TEVP fluids (stirred and unstirred yogurt, Carbopol, and Laponite), demonstrating that despite differences in microstructure, all three systems share a common underlying relationship between rheology and flow dynamics in the near wall region.

3.2 Rheological Modeling of Soft Matter using Artificial Neural Networks

Motivation

State of the art rheological predictions still rely heavily on constitutive modeling, where rheological properties are described through coupled, nonlinear differential equations that attempt to link microstructural dynamics to macroscopic stresses. Although decades of work have produced increasingly sophisticated models, such as Thixo-Viscoplastic (TVP) [64], Thixo-Elasto-Viscoplastic (TEVP) [19], and Iso-Kinematic Hardening (IKH) [42] frameworks, the number of parameters required to capture rate- and time-dependent behaviors grows rapidly, often reaching 10–15 parameters, many of which are difficult to measure and lack clear physical identifiability. As a result, even detailed constitutive equations frequently fail to reproduce experimental behavior across different flow protocols, especially when multiple lengthscales and timescales, or non-ideal physio- and bio-chemical effects dominate the response. Moreover, parameter fitting typically demands an exhaustive suite of experiments, and numerical implementation becomes cumbersome and computationally prohibitive as model complexity increases. These limitations have motivated the emergence of neural network based approaches. Unlike traditional models, data-driven frameworks can infer hidden rheological parameters from only a handful of experiments, and learn the underlying microstructural evolution of soft matter. Neural networks therefore offer a powerful and flexible alternative capable of overcoming the rigidity, parameter explosion, and limited predictive scope of classical constitutive modeling.

NARX Neural Network Architecture and Training

To evaluate the ability of data-driven models to reproduce the full transient rheological response of TEVP materials, a Nonlinear Autoregressive Neural Network with Exogenous Input (NARX) was trained using only the stress response from a multi-interval thixotropic test (MITT). After training, the same network was applied to a wide range of independent rheological experiments, to predict thixotropy, viscoelasticity, viscoplasticity and shear thinning behaviour of soft matter (commercially available yogurt in this case).

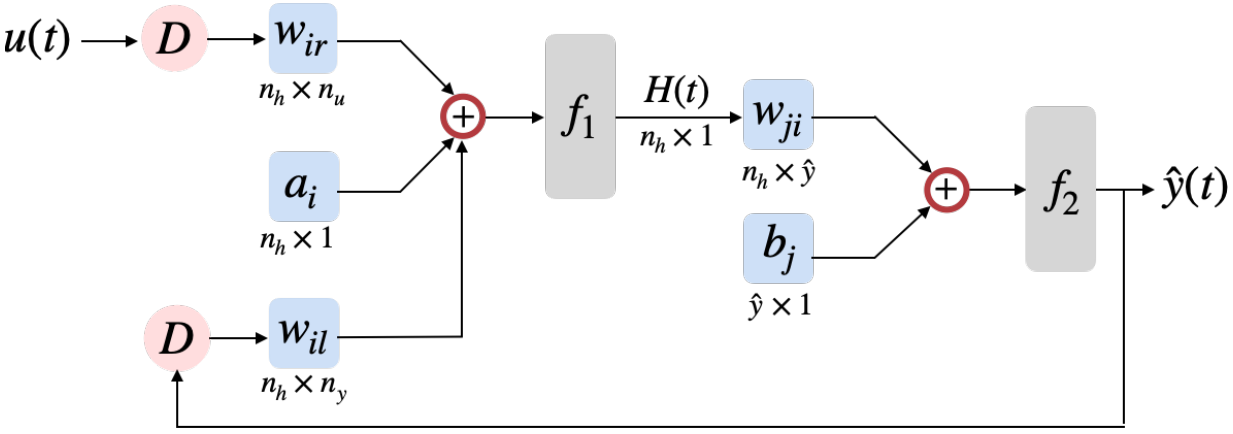

Figure 3.4: NARX neural network architecture.[61]

The NARX model used in this work is implemented in the open-loop configuration, following the architecture described by Mishra et al. [61]. The network receives the imposed time series of shear rate as the external (exogenous) input and uses the experimentally measured stress from previous time steps as the feedback signal during training. The use of input and output delays allows the NARX architecture to incorporate short-term shear history, which is essential for capturing rheological phenomena such as thixotropic structural rebuilding, viscoelastic phase lag, and yielding dynamics. After training, the same architecture is employed to generate predictions for new input shear rate histories.

Mathematically, the NARX model approximates the nonlinear mapping

$$\hat{\sigma}(t) = f(\dot{\gamma}(t), \dot{\gamma}(t-1), \ldots, \dot{\gamma}(t-n_u),\ \sigma(t-1), \ldots, \sigma(t-n_y))\,, \tag{3.6}$$

where past values of both the input (time series of shear rate, $\dot{\gamma}(t)$) and the output (time series of shear stress, $\sigma(t)$) are passed through a nonlinear hidden layer to predict the next stress value ($\hat{\sigma}(t)$). In this work, delays of 1:2 were used for both input (n_u) and output (n_y), and a single hidden layer of 10 neurons was found sufficient to capture the nonlinear dynamics without overfitting. Through this architecture, the network effectively learns how the internal structure of the material evolves in time as a function of both instantaneous shear and the preceding stress response.

The MITT dataset includes a sequence of alternating intervals in which the material undergoes structural breakdown at higher shear rates, corresponding to stresses above the yield stress, and partial recovery at lower shear rates, corresponding to stresses below the yield stress. 70% of the dataset was used for training, and 15% each for validation and testing purposes. The trained network reproduces the full transient stress response across all intervals with high accuracy ($\sim 98\%$), including subtle features such as partial recovery followed by renewed decay in the vicinity of the yield stress regime (Fig. 3.5(a)). This demonstrates that the model successfully internalizes short-timescale structural kinetics without requiring an explicit constitutive relation.

Rheological Predictions

The model predicts the viscoplastic behavior in Fig. 3.5(b) with over 99% accuracy. In stress-controlled steady-shear tests, the network identifies the onset of yielding and reproduces both the pre-yield viscosity plateau and the abrupt drop post yielding. In creep experiments (Fig. 3.5(c)), it captures the decrease in viscosity due to structural breakdown for $\sigma > \sigma_y$, increase in

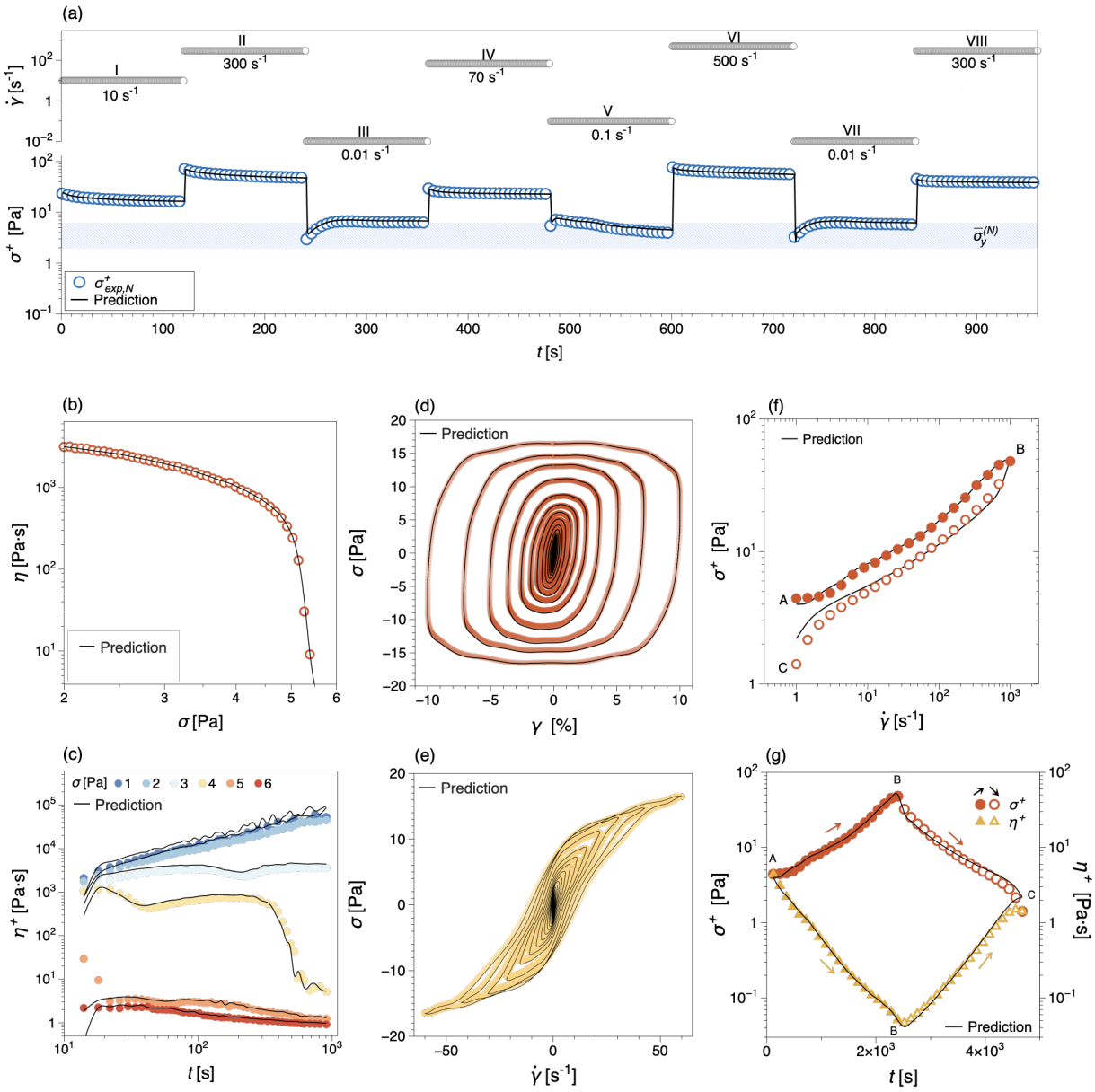

Figure 3.5: Figures showing NARX neural network trained on the (a) MITT dataset, and predictions of viscoplasticity in (b) stress controlled and (c) creep tests; predictions of viscoelasticity in (d-e) Lissajous–Bowditch curves; and thixotropy in shear rate controlled ramp up and down test plotted as (f) hysteresis loop, and as time evolution of (g) stress and viscosity. In all the figures, the symbols represent experimental dataset and black solid line represents NARX model predictions.

viscosity due to structural recovery for $\sigma < \sigma_y$, and the viscosity fluctuations near the yield stress threshold. Even subtle non-monotonic creep responses are reproduced, despite never being part of the training data.

In oscillatory shear predictions, the network reconstructs the full time-dependent stress response to sinusoidal strain inputs, yielding Lissajous - Bowditch curves that accurately reflect both linear and nonlinear viscoelastic behavior, with greater than 98% accuracy (Fig. 3.5 (d-e)). The model captures the phase lag, amplitude, and intra-cycle distortion, enabling extraction of G' and G'' across a wide range of strain amplitudes. These features emerge naturally from the learned mapping and do not rely on any explicit viscoelastic constitutive assumptions.

When applied to shear rate ramp tests, the trained model accurately reproduces both the ascending and descending branches of the thixotropic hysteresis loop (Fig. 3.5 (f-g)), with 92% accuracy. It captures the nonlinear increase in stress, the characteristic stress overshoot at low to mid shear rates, and the rate-dependent widening or narrowing of the loop.

Overall, these results show that a NARX network trained on a single transient shear rate controlled experiment is capable of reproducing the complete suite of rheological behaviors, including thixotropy, viscoelasticity, and viscoplasticity, that conventionally require multiple independent constitutive models. Furthermore, the NARX neural network can predict the rheological behaviour of other soft materials including Laponite, paint and emulsions, with unprecedented accuracy.

3.3 Soft Matter Flow in Circular Tubes

Rheological and Flow Experiments

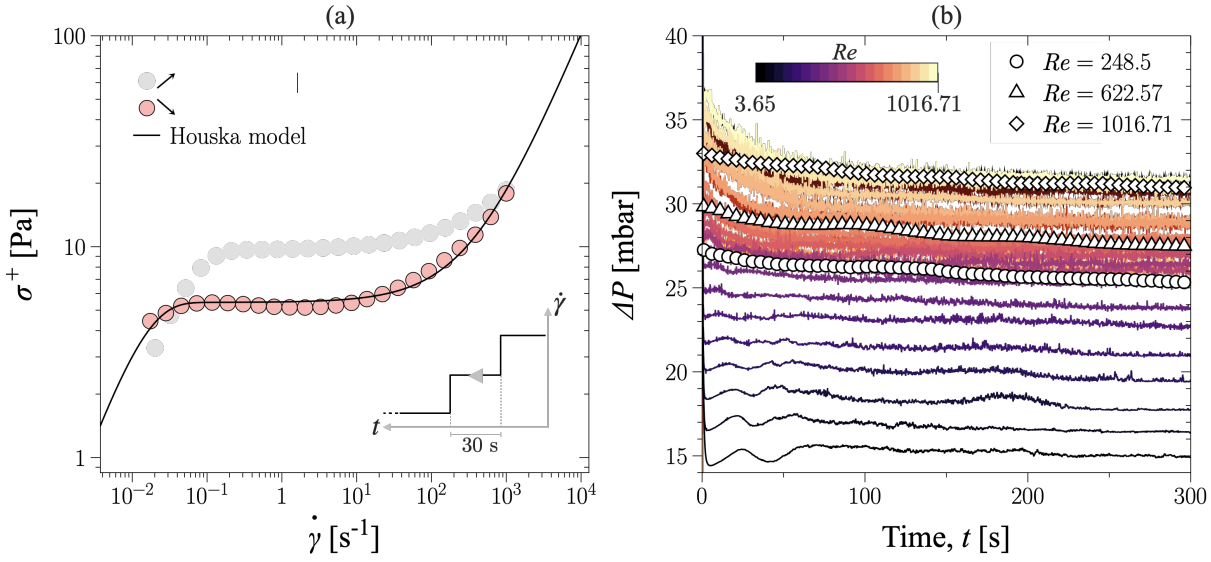

Figure 3.6: a) Steady state flow curve of a 2 wt% Laponite suspension measured in a rate-controlled shear ramp (30 s per time step). Grey symbols denote the upward shear rate sweep and pink symbols the downward sweep, revealing a pronounced thixotropic hysteresis loop. The solid line represents the Houska thixotropic model fitted to the downward ramp. The inset illustrates the stepped shear rate protocol used in the experiment. (b) Temporal evolution of the pressure drop (ΔP) measured in pipe flow at constant flow rates for a wide range of $Re \in [3.65, 1016.71]$. Symbols correspond to experimental measurements and curves are predictions from simulations, colour coded by Re.[58]

The flow curve of Laponite 2 wt % suspension was measured by performing a ramp down in shear rate from $\dot{\gamma} = 10^3\ s^{-1}$ to $\dot{\gamma} = 10^{-2}\ s^{-1}$, with a time step size of 30 s at each shear rate to achieve near steady-state (pink circles in Fig. 3.6(a)). The flow curve was fitted with the Houska thixotropic model (black solid line) to obtain the model parameters which were used for CFD simulations. The Houska model fits the flow curve with high accuracy and even captures the decline in stress below the critical shear rate. The grey

circles in Fig. 3.6(a) represent the ramp up curve of the hysteresis loop.

The transient pressure drop measurements (represented by hollow symbols in Fig. 3.6(b)) obtained from the custom pipe rig apparatus reveal the strong time-dependent behaviour of the Laponite suspension under constant flow rates. For all investigated flow conditions, the pressure drop is highest at flow initiation, reflecting the fully structured state of the material. As the fluid begins to shear, the internal network undergoes rapid breakdown, which is immediately manifested as a decay in the measured pressure signal. This decay is evident in Fig. 3.6(b), where higher Re correspond to larger initial pressure drops. At low Re, the pressure decreases only slightly over time, indicating that shear levels are insufficient to substantially disrupt the microstructure. In contrast, at intermediate and high Re, the pressure drop shows a pronounced decline within the first tens of seconds, followed by a gradual approach towards a quasi-steady state as breakdown and recovery processes equilibrate. The experimental trends across all flow rates consistently demonstrate that the unsteady pressure response is controlled by the kinetics of structural degradation and recovery under shear.

Computational Fluid Dynamics Simulations

CFD simulations incorporating the Houska thixotropic constitutive model were performed using parameters extracted from the steady-shear flow curve (Fig. 3.6(a)). The solid lines in Fig. 3.6(b) represent the transient pressure drop obtained from CFD simulations for $3.65 < Re < 1016.71$. The simulations successfully reproduced both the magnitude and time-dependent evolution of the pressure drop across the full range of flow rates with approx. 98% accuracy. In the beginning, the simulated pressure drop decay closely follows the experimentally measured values, capturing the rapid structural breakdown near the pipe wall where shear rates are highest. As time progresses, the model reproduces the slower, asymptotic decrease associated with progressive struc-

tural equilibration throughout the pipe cross section. The model predictions are most accurate in the intermediate Re regime, where the relative error remains very small. At the highest flow rates, slight deviations appear during the first 20–30 s of flow initiation, suggesting that the extremely rapid breakdown observed experimentally is difficult to fully capture. Nevertheless, the overall correspondence between experiment and simulation confirms that the Houska model, through its coupling of viscosity, yield stress, and a time-evolving structure parameter, captures the essential physics underlying the transient pressure response.

Neural Networks Predictions of Transient Pressure Drop

Building on the experimental and CFD datasets, a neural network surrogate model was developed to predict the time-dependent pressure drop solely from time and flow rate inputs. The model architecture, illustrated in Fig. 3.7(a), consists of three hidden layers with 128–128–64 neurons, enabling it to learn the nonlinear functional mapping ($\Delta P = f(t, Q)$). To quantify how much training data the model requires to generalize across the full flow rate domain, a comprehensive data efficiency study was performed. All possible combinations of the available flow rate datasets were tested, and the optimal subsets for each training size are summarized in Fig. 3.7(b). The analysis shows that accurate generalization can be achieved with as few as three or four representative datasets (each containing 300 s of data), particularly when these include a combination of low, intermediate, and high flow rates. This indicates that the network primarily learns the characteristic shape and time-dependence of the pressure drop decay, and then smoothly interpolates (and modestly extrapolates) across the full flow rate space.

When evaluated against the complete experimental and CFD dataset, the neural network predictions show excellent agreement with the true pressure drop curves across all 20 flow rates (Fig. 3.7(c-d)). The model reproduces both

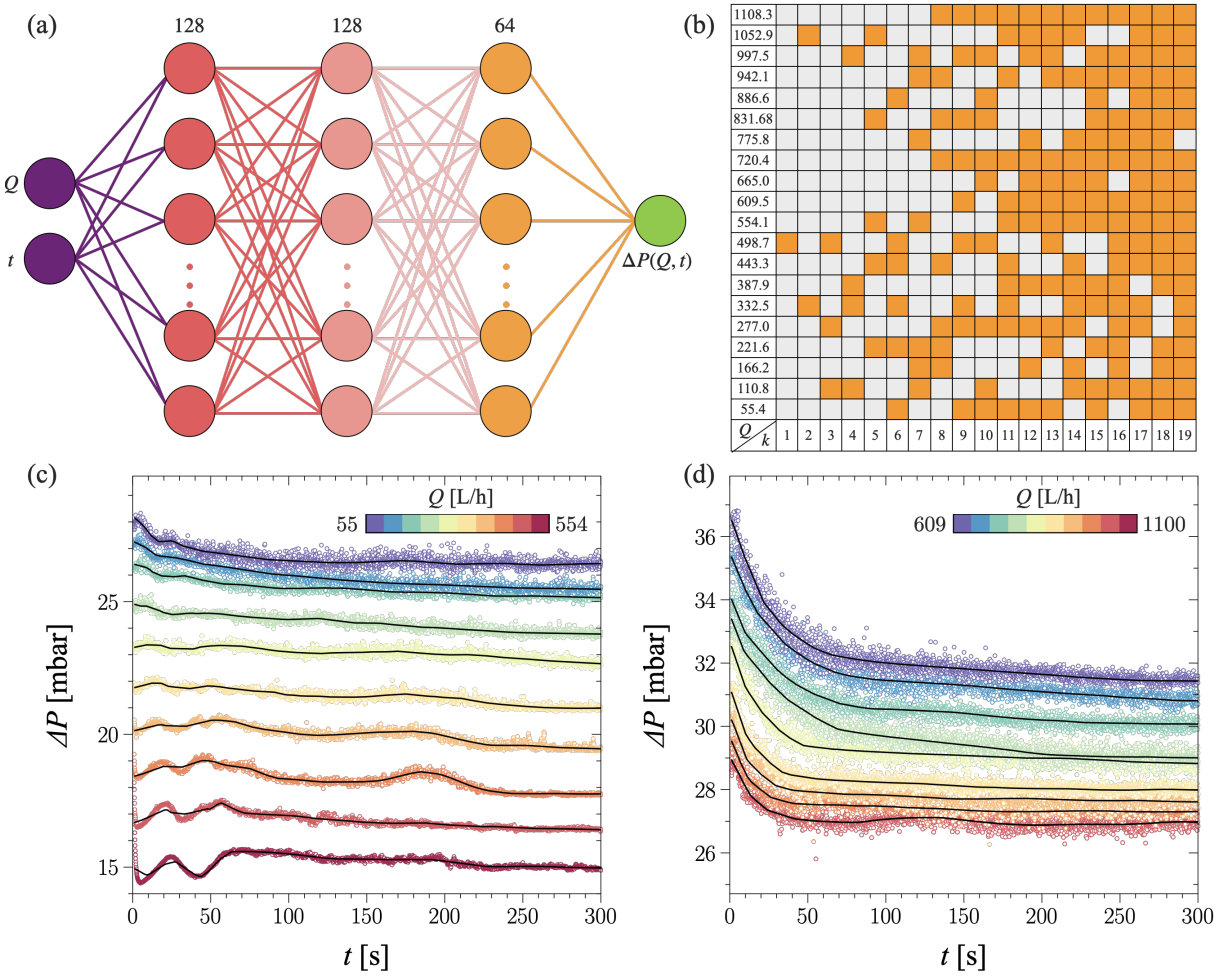

Figure 3.7: (a) Architecture of the fully connected feed-forward neural network used to predict the transient pressure drop, $\Delta P(Q, t)$, from flow rate Q and time t. The network consists of two inputs, three hidden layers with 128-128-64 neurons using ReLU activations, and a single linear output neuron. (b) Membership map showing the optimal training subset for each number of training flow rates k. Orange squares indicate inclusion of a given flow rate dataset in the best performing subset, demonstrating that representative low, intermediate, and high flow rates are essential for accurate generalization. (c,d) Comparison between experimental pressure drop data (colored markers) and neural network predictions (black curves) for flow rates spanning (c) 55-554 L/h and (d) 609-1100 L/h.[58]

the sharp initial decay and the slow time-dependent relaxation, and captures the systematic increase in pressure magnitude with flow rate. Small discrepancies appear primarily in the earliest transient regime, where experimental data is most sensitive to pump fluctuations. Despite this, the overall prediction error remains below 5% for all conditions, highlighting the effectiveness of the neural network as a surrogate for the full CFD model. Importantly, the network also maintains smoothness and physical consistency in its predictions, indicating that the training set successfully encodes the underlying thixotropic kinetics.

Together, the experimental measurements, CFD simulations, and neural network predictions provide a coherent and self consistent understanding of the transient pressure drop behaviour of thixotropic pipe flow. The experiments establish the fundamental phenomenon of shear-induced pressure decay with time, the CFD simulations predict the experiments and are used to create additional pressure drop datasets across a broader range of flow rates (without performing additional flow measurements), and the neural network offers a compact data-driven predictor capable of replacing computationally expensive and time consuming simulations with great accuracy. This integrated framework demonstrates how rheology, continuum modeling, and machine learning can be combined to describe, interpret, and predict the unsteady transport characteristics of thixotropic yield stress fluids.

3.4 3D Printing of Soft Matter

3D printing of soft matter relies critically on formulating materials whose flow behavior enables precise extrusion, shape retention, and structural fidelity. Such applications, ranging from bioprinting and soft robotics to food printing and functional materials, require materials that can flow easily through a nozzle yet immediately support their own weight once deposited. Achieving this balance is challenging because soft materials often exhibit complex elasto-viscoplastic behavior: they must possess sufficient yield stress to prevent dripping, strong shear-thinning to enable smooth extrusion, and controlled viscoelasticity to avoid excessive die swelling or spreading. Rheology therefore plays a central role in defining printability, governing how polymer networks deform under high shear inside the nozzle and relax upon exiting, ultimately dictating filament stability, layer adhesion, and final shape fidelity in extrusion-based additive manufacturing. Carbopol–PEO blends were selected because they form stable interpolymer networks in which Carbopol provides a tunable yield stress microgel structure, while PEO introduces controllable viscoelasticity. By adjusting the relative concentrations of Carbopol and PEO, the blend's yield stress, shear thinning behavior, and viscoelastic response can be systematically tuned, enabling precise control over extrusion and post-deposition flow in 3D printing applications. The extrusion behaviour of the Carbopol-PEO blends was examined by analyzing dimensionless flow parameters, die swelling, and the resulting print fidelity. This study provides a detailed picture of how viscoelasticity, surface tension, and yield stress govern the transition from droplet formation to stable filament extrusion, and ultimately determine the spread and width of printed strands.

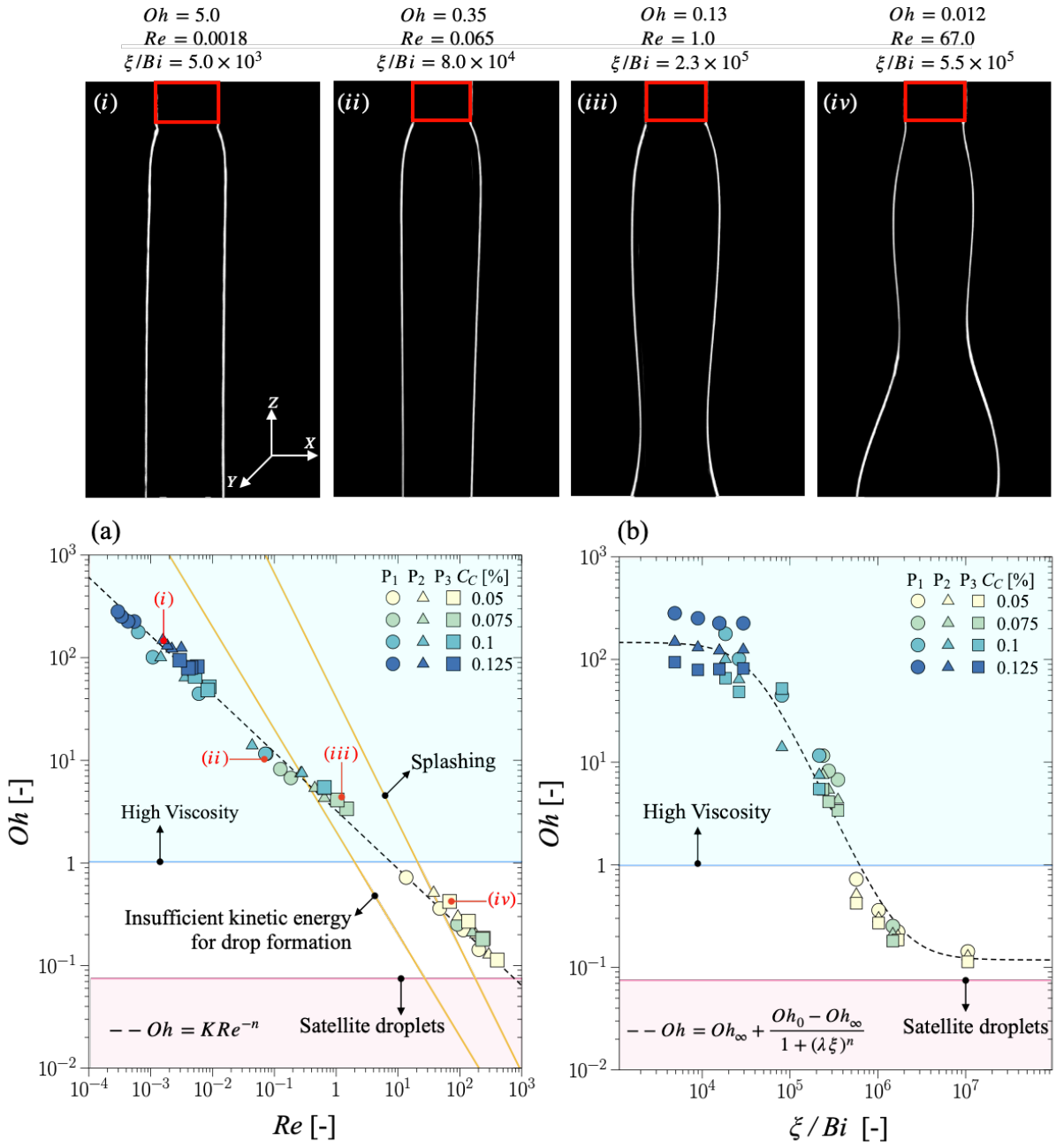

Figure 3.8: Flow regime classification and extrusion behavior of Carbopol–PEO blends during 3D printing. (Top) Representative extrusion snapshots illustrating the transition from stable filament formation to droplet breakup. (a) Variation of Oh with Re for all blend compositions and extrusion pressures, showing data collapse onto the power-law relation, $Oh = KRe^{-n}$. (b) Dependence of Oh on the modified Bingham number ξ/Bi, revealing a sigmoidal transition from viscoelastic dominated, droplet forming behavior at high ξ/Bi to yield stress dominated, filament forming behavior at low ξ/Bi.[59]

Dimensional Analysis of Die Swelling

Fig. 3.8(a) shows that the Ohnesorge number (Oh) decreases systematically with increasing Reynolds number (Re) across all compositions and extrusion pressures. The data collapse onto a power-law relation, $Oh = 3.2Re^{-0.57}$, indicating that the fluid behaviour is governed by a universal balance between viscous and inertial forces regardless of polymer concentration. At low Re (high viscosity), Oh exceeds unity and the blends fall within a regime dominated by viscous damping, where the extrudate forms a steady and continuous filament. As Re increases, the system transitions through intermediate values of Oh into a region where viscoelastic response and surface tension start to dominate. At $Oh < 0.07$, unstable extrusion behaviour is observed, with the onset of jet breaking up into droplets, consistent with snapshots (iii)–(iv) in Fig. 3.8. These regimes are in agreement with established criteria for inkjet printability, where very low Oh promotes satellite-drop formation, while excessively high Oh prevents droplet detachment altogether.

The modified Bingham number (ξ/Bi), shown in Fig. 3.8(b), further clarifies how viscoelasticity and yield stress interact to control flow stability. High values of ξ/Bi correspond to low yield stress and a strong tendency for the material to elastically recoil upon exiting the nozzle. In this regime, Oh rapidly drops and the extrudate becomes prone to pulsation and droplet formation. As ξ/Bi decreases, the increasing yield stress stabilizes the jet and suppresses breakup, as reflected in the sigmoidal relationship between Oh and ξ/Bi. This sigmoidal curve effectively delineates the threshold between viscoelastic dominated fluid behaviour (droplet forming, snapshots (iii)–(iv) in Fig. 3.8) and yield stress dominated behaviour (filament forming, snapshots (i)–(ii) in Fig. 3.8). Compositions with $\xi/Bi \leq 8 \times 10^4$ and $Oh \geq 10^2$ consistently produce stable filaments suitable for extrusion-based 3D printing.

The influence of these dimensionless parameters on die swelling is captured

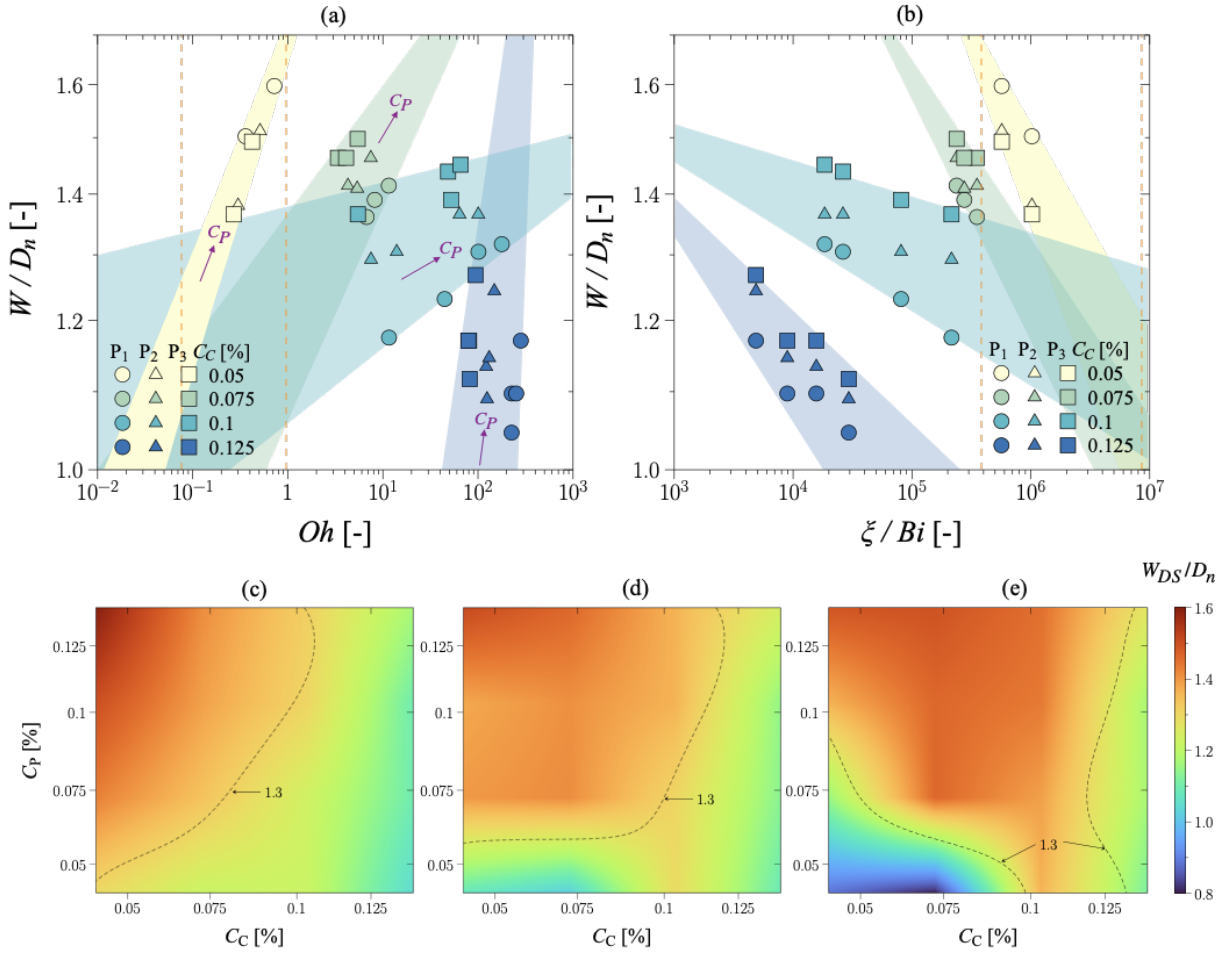

Figure 3.9: Die swell behavior of Carbopol–PEO blends as a function of rheological dimensionless groups and composition. (a) The die swell ratio W/D_n increases sharply with decreasing Ohnesorge number (Oh), indicating enhanced elastic recoil and reduced yield stress at low Oh. (b) A similar dependence is observed with the modified Bingham number ξ/Bi, where high ξ/Bi (low yield stress) leads to pronounced swelling, while low ξ/Bi suppresses relaxation. (c–e) Composition maps of the die swell ratio show that high PEO and low Carbopol contents produce the strongest swelling, reaching up to $1.6D_n$, whereas increasing Carbopol concentration introduces network jamming that limits transverse expansion. Increasing extrusion pressure increases die swell, as higher shear within the nozzle enhances chain stretching and increases the driving force for recoil upon exit.[59]

in Fig. 3.9. The die swell ratio (W/D_n) increases sharply as Oh decreases (Fig. 3.9(a)), revealing a strong sensitivity of post-extrusion expansion to the balance between viscous and surface tension forces. At low Oh, reduced viscous damping coupled with low yield stress allows the polymer network to fully relax upon exiting the nozzle, producing substantial radial recoil and transverse expansion. This regime corresponds to blends where viscoelasticity dominates, and even minor changes in composition can lead to pronounced differences in swelling behavior. In contrast, at high Oh (viscosity-dominated), elastic relaxation is strongly suppressed, and die swell remains minimal across all compositions. The dependence of die swell on ξ/Bi (Fig. 3.9(b)) mirrors these trends: high ξ/Bi indicating low yield stress and high elastic contribution leads to pronounced swelling, whereas low ξ/Bi (high yield stress) constrains polymer mobility and limits the ability of the extrudate to expand. The decrease of die swell with decreasing ξ/Bi highlights the competitive interplay between elastic recoil and yield stress–induced structural rigidity. Materials with high ξ/Bi values fall into a regime where elasticity and surface tension dominate the exit flow, whereas those with low ξ/Bi transition into a jammed, yield stress controlled state that attenuates swelling.

Fig. 3.9(c–e) maps the die swell ratio across the full composition space at different extrusion pressures, providing a more complete picture of how Carbopol–PEO interactions govern post-extrusion behavior. At low Carbopol concentrations, die swell is strongly amplified by increasing PEO content, reaching values up to 1.6 times the nozzle diameter. This behavior is characteristic of systems with negligible yield stress, where PEO-driven elasticity and chain relaxation govern the expansion. As Carbopol concentration increases, the system becomes increasingly jammed, suppressing relaxation and reducing die swell even when PEO is present. The contour maps highlight a distinct transition boundary between viscoelasticity-dominated and yield stress–dominated regions, demonstrating how small changes in composition shift the material

between these regimes. Notably, higher extrusion pressures shift the entire die swell landscape toward greater swelling (Fig. 3.9(c) to (e)). Elevated pressure increases the shear rate inside the nozzle, stretching both the Carbopol microgel network and the PEO chains to a greater extent. This pre-stretching creates a stronger driving force for recoil at the exit, amplifying the expansion even in compositions that would otherwise exhibit moderate or minimal swelling. Overall, the combined influence of Oh, ξ/Bi, composition, and extrusion pressure reveals a coherent physical picture: die swell is maximized when viscosity and yield stress are low, elasticity is high, and shear-induced polymer chain expansion is significant.

Influence of Die Swelling on Print Fidelity

The impact of die swelling on material deposition during 3D printing is illustrated in Fig. 3.10. The normalized print width (W_P/D_n) scales linearly with the die swell ratio (W_{DS}/D_n), demonstrating that the swelling of the extrudate in air, prior to deposition, is detrimental to lateral spreading on the substrate. However, the degree of spreading is strongly modulated by Oh. At high $Oh > 10^2$, spreading remains small and well-controlled, producing printed lines only slightly wider than the nozzle (Fig. 3.10(b), snapshots (i)-(ii)). In the intermediate regime ($1 < Oh < 10^2$), die swell is moderate and the printed strands exhibit noticeable spreading, producing widths up to three to four times the nozzle diameter (Fig. 3.10(b), snapshots (iii)-(iv)). In contrast, for $Oh < 1$, the combined effects of low viscosity, low yield stress, and high viscoelastic recoil cause extensive spreading after deposition, yielding widths up to six to seven times the nozzle diameter (Fig. 3.10(b), snapshots (v)-(vii)). Some compositions in low Oh regime cannot sustain continuous printing and instead exhibit dripping or droplet deposition.

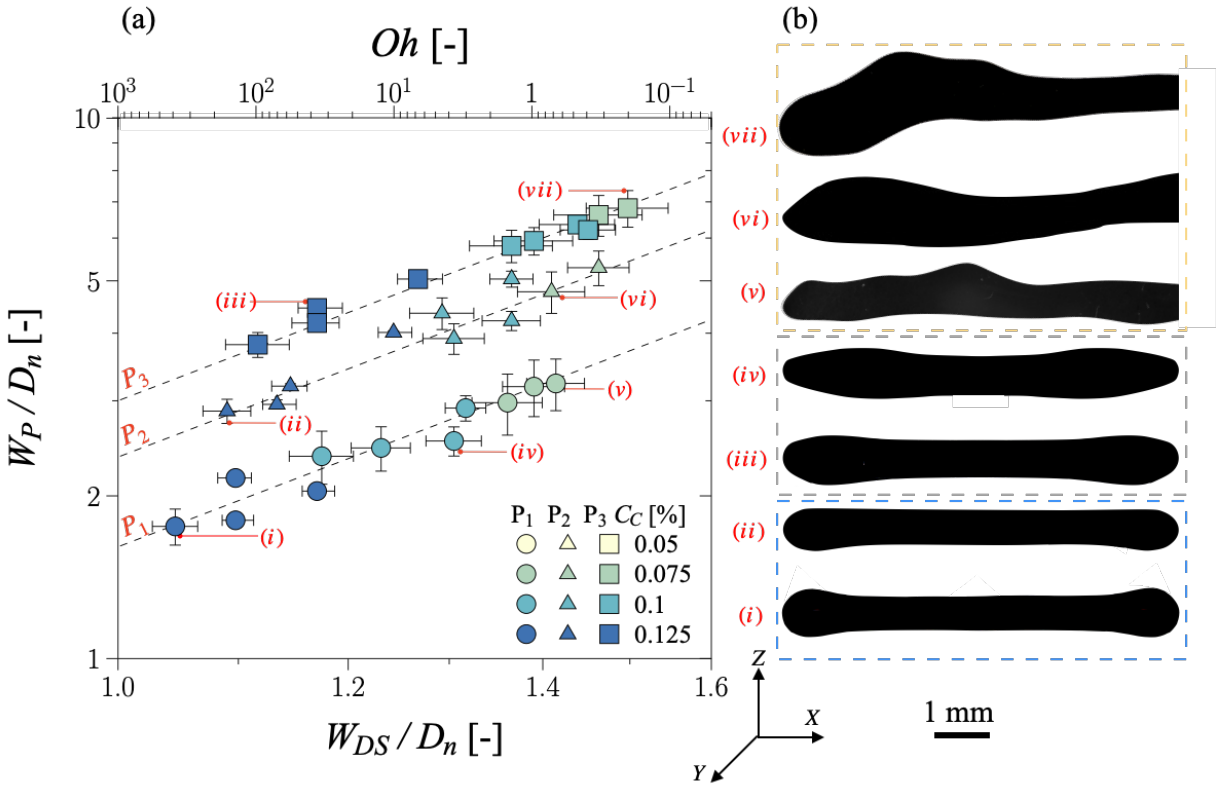

Figure 3.10: Effect of die swell on printed filament width. (a) The normalized print width W_P/D_n increases linearly with the die-swell ratio W_{DS}/D_n, showing that extrudate expansion in air directly enlarges deposited strand width. (b) Snapshots (i)-(vii) illustrate that spreading is minimal at high Oh, grows at intermediate Oh, and becomes extensive for low $Oh < 1$, where low viscosity and low yield stress promote strong recoil and, in some cases, dripping instead of continuous printing.[59]

Structural Insights

Rheo-SAXS measurements were carried out to resolve how microstructural features evolve in neat Carbopol, neat PEO, and their blends, with the goal of identifying length scales relevant to post-extrusion swelling. The results are summarized in Fig. 3.11. Guinier analysis of the azimuthally averaged scattering profiles (performed on the final ten frames of the relaxation step) yielded an effective radius of gyration, R_g, which reflects different structural characteristics depending on composition: polymer coil dimensions in dilute PEO solutions, microgel mesh size in Carbopol dispersions, and a correlation length describing spatial density fluctuations in the blended networks. In neat PEO, R_g captures the expected coil size, whereas Carbopol samples exhibit a nearly constant R_g, consistent with a fixed microgel mesh size even as concentration increases. Although yield stress rises sharply with increasing Carbopol content, the SAXS patterns remained isotropic, indicating that any shear-induced orientation had relaxed by the time of measurement. In the blends, small additions of PEO at low Carbopol levels increase the correlation length, consistent with hydrogen-bond-driven expansion of the network. At higher Carbopol concentrations, low PEO levels reduce yield stress, likely due to PEO mediated softening of microgel-microgel contacts. Whereas larger PEO additions reintroduce jamming, accompanied by increases in both yield stress and R_g. The highest correlation length was observed for the sample with $C_C = 0.05$ wt% and $C_P = 0.125$ wt%, which also exhibited the strongest die swelling, suggesting that swelling scales with the correlation length. These results indicate that R_g reflects the average spacing between microgels modulated by PEO, with larger values corresponding to more PEO-rich regions capable of enhanced relaxation and, consequently, greater post-extrusion expansion.

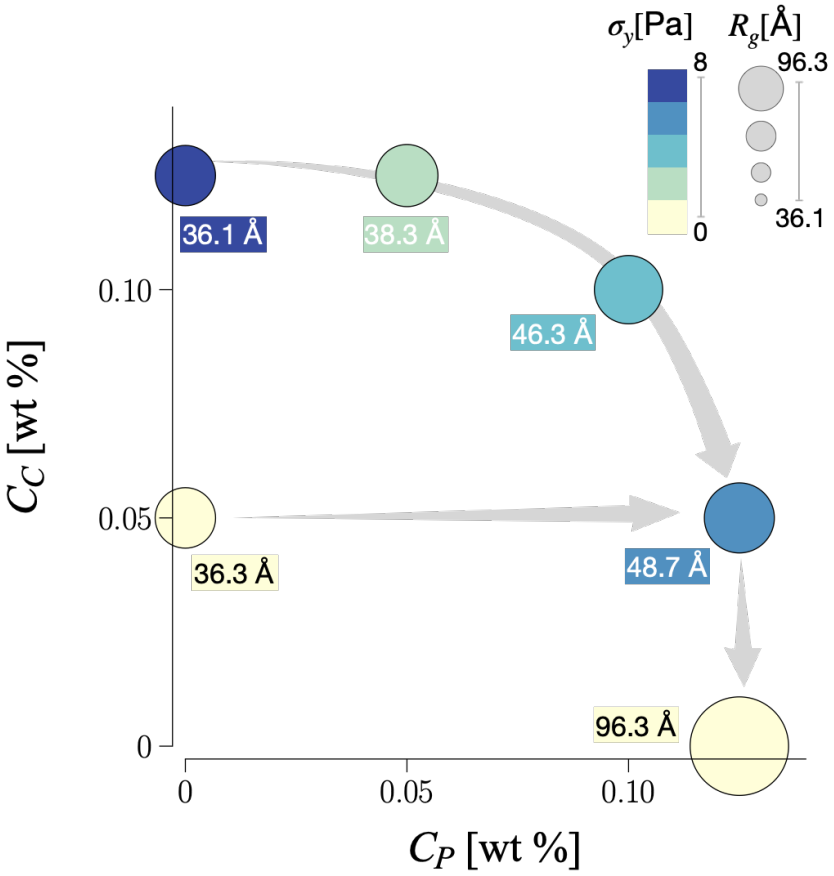

Figure 3.11: Figure illustrating the variation of the effective radius of gyration, R_g, across different Carbopol and PEO concentrations. The size of each symbol reflects the magnitude of R_g, while the color scale represents the corresponding yield stress. Labels indicate the extracted R_g values. Depending on the formulation, R_g may represent the polymer coil radius of gyration (PEO), the microgel mesh size (Carbopol), or the correlation length characterizing the blended systems.[59]

3.5 Rheology of Bio-based Soft Matter: Human Saliva

Saliva is well established as a viscoelastic biologically relevant fluid whose rheological properties play a central role in oral health. Altered salivary viscoelasticity has been reported in a number of conditions, including Sjögren's syndrome [65], xerostomia [66], radiation-induced hyposalivation [67], [68], cystic fibrosis [69], diabetes mellitus [70], and several chronic oral mucosal disorders [71], [72]. These conditions often involve compromised lubrication, impaired bolus formation, and reduced mucosal protection—functions that could be directly influenced by the rheological properties of saliva. Motivated by these clinical aspects, we examined whether saliva also exhibits thixotropic behaviour, an important rheological property that remains largely unexplored in oral physiology. In particular, we investigate whether the extent of thixotropy shows any relationship with salivary secretion rate, a parameter strongly associated with the onset and severity of xerostomia.

Shear and Oscillatory Rheology

The rheological characterization of unstimulated (US) and stimulated (S) whole saliva samples reveals a pronounced dependence on both secretion rate and biochemical composition. Unstimulated saliva consistently exhibits higher viscosities across the shear-rate range. This behaviour is attributed to the elevated concentration of mucins, particularly the high molecular weight MUC5B and the lower molecular weight MUC7, which dominate unstimulated saliva composition and impart enhanced cohesive and viscoelastic properties. Quantitatively, viscosities of unstimulated saliva span approximately 2–20 mPa·s, whereas stimulated saliva ranges between 1–8 mPa·s. Power-law fits confirm this difference: the consistency index (K) is roughly twice as high for unstimulated saliva, while the flow index (n) indicates slightly more pronounced shear thinning behaviour. The microstructural implications of these viscosity

trends become evident when examining the oscillatory shear response. Across all samples, the storage modulus exceeds the loss modulus over the entire accessible frequency range, indicating a gel-like character with long relaxation times. Although both saliva types display comparable frequency dependence, unstimulated saliva shows systematically higher values of (G') and (G''), consistent with a denser mucin network. Notably, the viscoelastic properties correlate positively with both calcium and glycoprotein concentration in unstimulated saliva. This is in accordance with molecular insights: calcium ions promote the unfolding and reversible cross-linking of MUC5B, increasing its capacity for water retention and structural entanglement.

Time-Dependent Rheology

We have found that human saliva is thixotropic in nature due to its biochemical composition. A more comprehensive view of the time-dependent material behaviour emerges from the thixotropic hysteresis loops included in Fig. 3.12. Both saliva types exhibit marked hysteresis, but the magnitude of the loop area is significantly larger in unstimulated saliva, reflecting its higher mucin content and thixotropy (Fig. 3.12(a-b)). A clear stress overshoot appears at low to intermediate shear rates during the upward ramp. This overshoot is consistent with the disentanglement of long-chain mucins: initially, polymer networks resist deformation elastically, producing a peak in stress. Subsequently, alignment and progressive breakdown of the mucin structures lead to a stress drop. At high shear rates the fluid approaches a fully disrupted state, dominated by aligned and partially degraded polymer structures. Upon decreasing the shear rate, partial recovery of the mucin network becomes evident, although complete structural rebuilding requires rest. The qualitative evolution of this microstructure, schematically illustrated in Fig. 3.12(c), highlights the roles of molecular entanglement, chain stretching, alignment, and the adsorbed protein layer at the saliva–air interface. The latter provides an

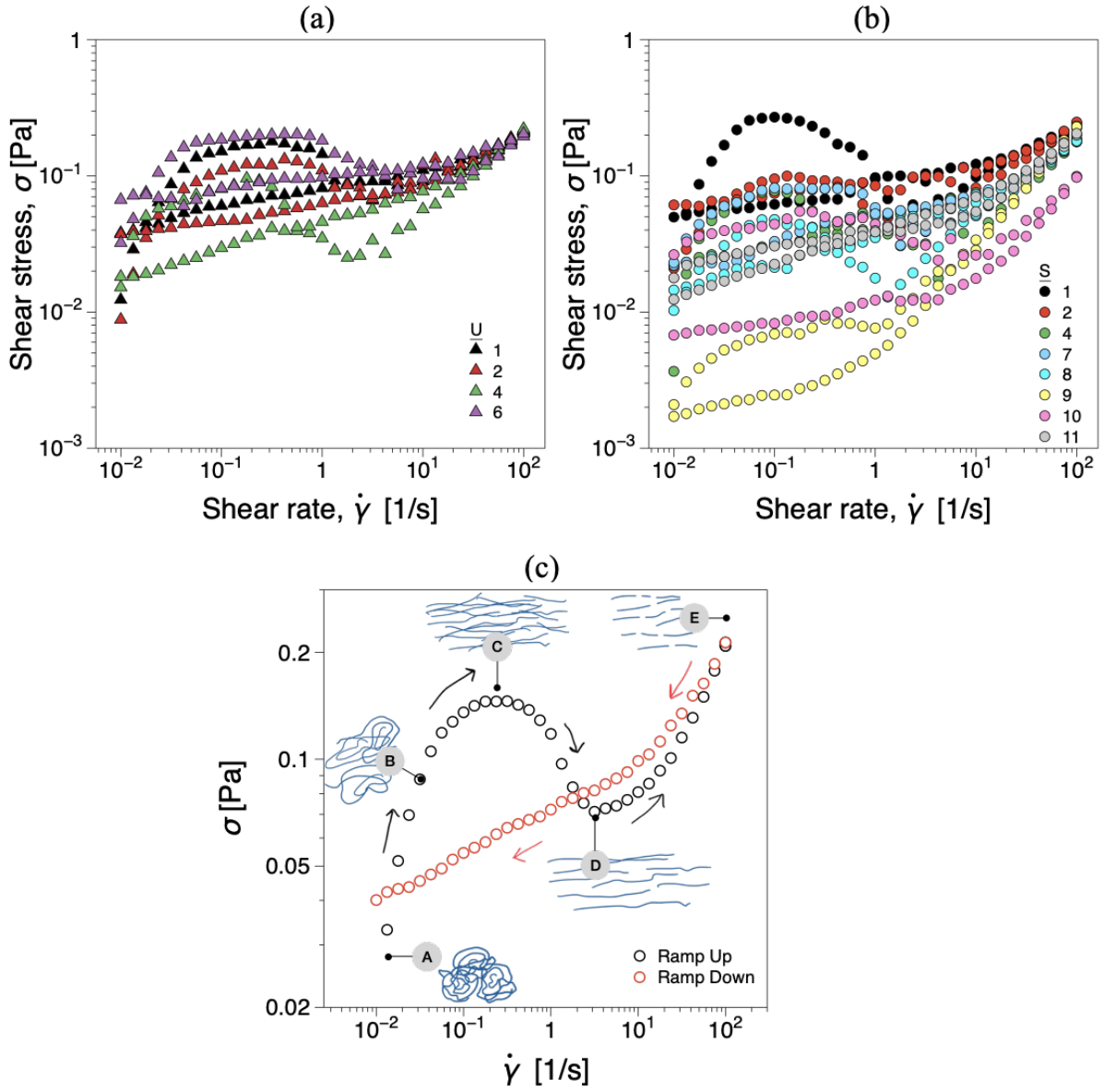

Figure 3.12: Figues showing thixotropy of human saliva samples in hysteresis loop measured by shear rate ramp up and down test for (a) unstimulated and (b) stimulated saliva. (c) Typical stress evolution in saliva showing self-intersecting hysteresis loop, marked with structural states (A-E) along the ramp up curve.[62]

additional contribution to the stress response at high shear rates and may explain the self-intersection of hysteresis curves, a behaviour commonly seen in soft glassy materials. Building on the schematic structural evolution, the thixotropic loop can be interpreted through the sequence of microstructural states labeled A–E in Fig. 3.12(c). At point A, saliva is in a highly entangled, quasi-equilibrium state dominated by large MUC5B-rich aggregates and clusters of interacting mucin chains. Moving from A to B, the onset of shear causes these long-chain mucins to stretch and partially disentangle, producing an initial rise in stress associated with elastic deformation of the network. Between B and C, continued shear promotes further disentanglement and alignment of the mucin chains, leading to the characteristic stress overshoot. From C to D, the system transitions toward a more flow-aligned state: aggregates are broken down, the network connectivity decreases, and the stress begins to decay as viscosity drops. Finally, from points D to E, continued shear thinning leads to extensive disruption of the mucin network, resulting in predominantly individual or weakly interacting chains that are fully aligned with the flow direction. During the downward ramp, partial reformation of intermolecular associations occurs only slowly due to the long relaxation times of MUC5B, producing the pronounced hysteresis and highlighting the inherently time-dependent recovery of saliva's microstructure.

Scaling Laws

To consolidate the contributions of viscosity, viscoelasticity, and thixotropy into a unified framework, rheological parameters were combined into a dimensionless quantity, the Sialo number (Π). This parameter integrates the consistency and flow indices from shear thinning behaviour, the viscoelastic factor ($G = G' - G''$), the thixotropic loop area (S_y), age of the patient, volume of the sample collected, and the secretion rate. The resulting dependence of Π on secretion rate is shown in Fig. 3.13. A striking feature is that

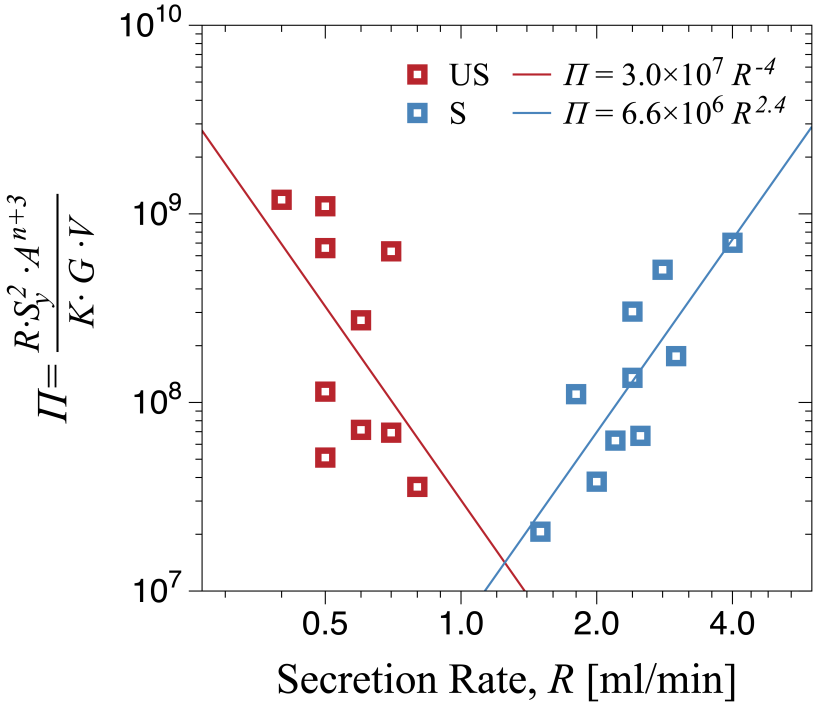

Figure 3.13: Scaling laws relating saliva secretion rate to rheological parameters. [62]

unstimulated and stimulated saliva exhibit fundamentally opposite scaling behaviour. For unstimulated saliva, Π decreases with increasing secretion rate following a negative power law. This reflects the strong thixotropic response at low secretion rates, where the high concentration of slow-relaxing MUC5B-rich networks produces large hysteresis areas S_y, and therefore large Π. As the secretion rate increases, the degree of structural buildup decreases, leading to smaller S_y and a corresponding reduction in Π. In contrast, for stimulated saliva, Π increases with secretion rate according to a positive power law. In this case, the lower mucin content, together with the smaller values of the consistency index and the viscoelastic factor, facilitates an increase in Π with the secretion rate..

The power-law relationships suggest that secretion rate is a primary deter-

minant of the interplay between structural, biochemical, and flow-dependent properties of saliva. Because the thixotropic loop area (S_y) enters quadratically in the Sialo number, thixotropy emerges as the dominant rheological parameter governing the scaling behaviour. The long relaxation times associated with high molecular weight mucins govern the time-dependent mechanical response of saliva. Secretion rates below approximately 0.2 ml/min fall in a regime associated with reduced secretion rate and has been linked clinically to sensations of oral dryness or xerostomia.

CHAPTER 4

Conclusions, and future work

4.1 Conclusions

The work presented in this thesis establishes a unified and multi-scale framework for understanding, modeling, and predicting the flow behaviour of thixo-elasto-viscoplastic (TEVP) soft materials. By bringing together controlled rheological experiments, microstructural characterization, spatially resolved flow measurements, constitutive and structural-kinetic modeling, computational fluid dynamics (CFD), and neural network-based data-driven tools, this thesis demonstrates how interdisciplinary methodologies can overcome long-standing challenges in the study of time-dependent soft matter.

Across all material systems examined, the results show that TEVP flow behaviour originates from the evolving microstructure and the coupled contributions of viscoelasticity, yield stress, and thixotropy. Rheological tests uncover distinct signatures of structural breakdown and recovery, providing

critical insight into how the material reorganizes under flow. These measurements provide the fundamental material functions required to parameterize predictive models and to interpret flow behaviour in various geometries with accuracy. Flow-resolved imaging using Doppler optical coherence tomography (D-OCT) enabled, for the first time, a direct comparison between bulk rheology and the spatial development of flow fields in millifluidic channels. Velocity profiles captured the formation of plug regions, wall slip, and shear localization, illustrating how even subtle differences in microstructure or thixotropic kinetics manifest as distinct flow signatures. Pipe flow experiments further demonstrated that TEVP fluids exhibit marked transient behaviour, where pressure drop evolution reflects the competition between structural rebuilding at low shear and shear-induced breakdown at higher rates. By coupling these measurements with structural kinetic models and CFD simulations, the thesis provides a quantitative description of unsteady TEVP transport and clarifies the evolution of structural parameters within complex flow fields. A major contribution of the thesis lies in the development and deployment of neural network-based predictive frameworks. The NARX-based digital rheometer shows that minimal experimental input, often a single transient test, is sufficient to reconstruct a wide range of rheological behaviours, overcoming limitations of classical constitutive models that rely on numerous, often unidentifiable parameters. Similarly, neural network flow surrogates for pipe flow capture transient pressure signatures with high accuracy and drastically reduced computational cost. These results illustrate how machine learning can complement and extend continuum modeling, offering flexible alternatives for rheology reconstruction and flow prediction when traditional models become under-determined or computationally prohibitive. The thesis also advances the understanding of extrusion and 3D printing of soft matter. Using rheology, dimensional analysis, high-speed imaging, and structural probes such as Rheo-SAXS, the work identifies how viscoelasticity, yield stress, and interfacial

forces jointly govern die swell, filament formation, and print fidelity. These insights contribute practical design rules for selecting or engineering printable polymer blends and demonstrate how multi-scale structural changes influence macroscopic print outcomes. In addition, the thesis demonstrates for the first time that human saliva is distinctly thixotropic, beyond its well-known viscoelastic properties. Through newly derived scaling laws, we reveal how this time-dependent structural evolution governs the relationship between rheology and secretion rate, offering new insight into the physiological origins of xerostomia and the conditions that exacerbate dry-mouth symptoms.

The contributions of this thesis demonstrate that reliable prediction of TEVP behaviour requires synergies between experiments, microstructure-aware constitutive modeling, flow-resolved measurements, CFD, and neural networks. By integrating these components, the thesis provides new mechanistic insights, resolves persistent challenges related to model selection and parameter identifiability, and delivers computationally efficient tools for engineering, processing, and formulation of soft materials. The methodology developed here bridges the gap between measured and predicted soft-matter behaviour, enabling more accurate and robust design of processes involving thixotropic yield stress fluids across industrial, technological, and biomedical contexts.

4.2 Potential for Future Work

The findings of this thesis open several promising avenues for advancing the predictive understanding and practical use of thixo-elasto-viscoplastic (TEVP) soft materials. Building on the integrated experimental–computational–data-driven framework developed here, future research may progress along the following directions.

Hybrid data-driven and physics-based constitutive modeling

Future work can merge physics-informed neural networks (PINNs), rheology-informed neural networks (RhINNs), and structural-kinetic constitutive models into unified hybrid frameworks. Such approaches would enable robust inference of microstructural parameters, relaxation spectra, and thixotropic kinetics directly from multimodal datasets (e.g. stress signals, velocity fields, OCT, SAXS) while enforcing physical constraints, thereby reducing reliance on extensive rheological testing, flow measurements and structural characterization.

Microstructure-flow imaging in complex geometries

The D-OCT approach demonstrated here may be extended to curved, converging, or porous geometries, ideally in combination with confocal microscopy or scattering techniques. These methods would allow direct observation of local yielding, shear banding, and plug development, providing rich datasets for validating TEVP constitutive and kinetic models under realistic processing conditions. Future efforts may exploit the scaling laws and structure–flow correlations identified here to guide formulation of soft materials with targeted viscoelasticity, yield stress, and thixotropy. This includes optimizing 3D-printable inks, lubricants, and gels for stability and processability, with microstructural descriptors serving as tunable design parameters.

Three-dimensional TEVP flow simulation tools

Advancing beyond pipe flow, future work could develop GPU-accelerated CFD solvers for full 3D geometries such as mixers, extrusion dies, and microfluidic networks. Incorporating spatially varying structural parameters, wall slip, and transient kinetic equations would enable predictive design and optimization of industrial processing operations involving TEVP materials.

Biologically relevant TEVP systems

The discovery that human saliva is strongly thixotropic, in addition to its well-known viscoelasticity, opens new biomedical directions. Future work may examine how thixotropy varies with age, hydration, medication, and diseases; explore saliva rheology in conditions such as diabetes, cystic fibrosis, and radiation-induced dysfunction; and link time-dependent rheological signatures to biochemical composition. Integrating these insights with machine learning and physiologically informed flow models may establish saliva rheology as a diagnostic or prognostic tool for disorders involving impaired lubrication.

Toward a unified TEVP framework

Finally, the combined insights of this thesis motivate efforts toward a generalized theoretical description of TEVP soft matter. This may include identifying universal scaling parameters, developing microstructure-aware constitutive models, and exploring structure–field coupling principles that apply across all soft matter systems.

References

[1] R. G. Larson, *The Structure and Rheology of Complex Fluids*. New York: Oxford University Press, 1999, ISBN: 9780195121971.

[2] D. Bonn, M. M. Denn, L. Berthier, T. Divoux, and S. Manneville, "Yield stress materials in soft condensed matter," *Reviews of Modern Physics*, vol. 89, no. 3, p. 035 005, 2017.

[3] J. Mewis, "Thixotropy-a general review," *Journal of Non-Newtonian Fluid Mechanics*, vol. 6, no. 1, pp. 1–20, 1979.

[4] G. Ovarlez, Q. Barral, and P. Coussot, "Three-dimensional jamming and flows of soft glassy materials," *Nature materials*, vol. 9, no. 2, pp. 115–119, 2010.

[5] A. Mujumdar, A. N. Beris, and A. B. Metzner, "Transient phenomena in thixotropic systems," *Journal of Non-Newtonian Fluid Mechanics*, vol. 102, no. 2, pp. 157–178, 2002.

[6] C. W. Macosko, "Rheology principles," *Measurements and Applications*, 1994.

[7] R. B. Bird, R. C. Armstrong, and O. Hassager, "Dynamics of polymeric liquids. vol. 1: Fluid mechanics," 1987.

[8] M. Crochet, "Numerical simulation of viscoelastic flow," *Lecture series-van Kareman Institute for fluid dynamics*, vol. 3, A1–A68, 1994.

[9] M. A. Rao, "Viscoelastic properties," *Rheology of Fluid and Semisolid Foods: Principles and Applications*, p. 59, 2010.

[10] T. M. Squires and S. R. Quake, "Microfluidics: Fluid physics at the nanoliter scale," *Reviews of modern physics*, vol. 77, no. 3, pp. 977–1026, 2005.

[11] P.-G. De Gennes, "Soft matter," *Science*, vol. 256, no. 5056, pp. 495–497, 1992.

[12] H. A. Barnes, "Thixotropy—a review," *Journal of Non-Newtonian fluid mechanics*, vol. 70, no. 1-2, pp. 1–33, 1997.

[13] P. Coussot, "Yield stress fluid flows: A review of experimental data," *Journal of Non-Newtonian Fluid Mechanics*, vol. 211, pp. 31–49, 2014.

[14] P. Coussot, "Fifty shades of yield stress fluids: Rheological challenges and engineering perspectives," *Rheologica Acta*, pp. 1–27, 2025.

[15] A. Y. Malkin, S. R. Derkach, and V. G. Kulichikhin, "Rheology of gels and yielding liquids," *Gels*, vol. 9, no. 9, p. 715, 2023.

[16] J. Mewis and N. J. Wagner, *Colloidal suspension rheology*. Cambridge university press, 2012.

[17] M. Dinkgreve, J. Paredes, M. M. Denn, and D. Bonn, "On different ways of measuring "the" yield stress," *Journal of non-Newtonian fluid mechanics*, vol. 238, pp. 233–241, 2016.

[18] P. Møller, A. Fall, and D. Bonn, "Origin of apparent viscosity in yield stress fluids below yielding," *Europhysics Letters*, vol. 87, no. 3, p. 38 004, 2009.

[19] D. De Kee, "Yield stress measurement techniques: A review," *Physics of Fluids*, vol. 33, no. 11, 2021.

[20] M. Larsson, J. Duffy, and M. AB, "An overview of measurement techniques for determination of yield stress," *Annu. Trans. Nord. Rheol. Soc*, vol. 21, pp. 125–138, 2013.

[21] A. B. Howard, "The yield stress-a review or panta roi-everything flows," *J. Non-Newtonian Fluid Mech*, vol. 81, pp. 133–178, 1999.

[22] J. D. Ferry, *Viscoelastic properties of polymers*. John Wiley & Sons, 1980.

[23] P. Sollich, F. Lequeux, P. Hébraud, and M. E. Cates, "Rheology of soft glassy materials," *Physical review letters*, vol. 78, no. 10, p. 2020, 1997.

[24] K. Hyun et al., "A review of nonlinear oscillatory shear tests: Analysis and application of large amplitude oscillatory shear (laos)," *Progress in polymer science*, vol. 36, no. 12, pp. 1697–1753, 2011.

[25] R. H. Ewoldt, A. Hosoi, and G. H. McKinley, "New measures for characterizing nonlinear viscoelasticity in large amplitude oscillatory shear," *Journal of Rheology*, vol. 52, no. 6, pp. 1427–1458, 2008.

[26] M. L. Falk and J. S. Langer, "Dynamics of viscoplastic deformation in amorphous solids," *Physical Review E*, vol. 57, no. 6, p. 7192, 1998.

[27] P. Schall, D. A. Weitz, and F. Spaepen, "Structural rearrangements that govern flow in colloidal glasses," *Science*, vol. 318, no. 5858, pp. 1895–1899, 2007.

[28] K. Hyun, S. H. Kim, K. H. Ahn, and S. J. Lee, "Large amplitude oscillatory shear as a way to classify the complex fluids," *Journal of Non-Newtonian Fluid Mechanics*, vol. 107, no. 1-3, pp. 51–65, 2002.

[29] C. Roberto and T. Véronique, "Introduction to viscoelasticity and plasticity, and their relation to the underlying microscopic dynamics in soft matter systems," *Physica A: Statistical Mechanics and its Applications*, vol. 631, p. 128 653, 2023.

[30] J. Mewis and N. J. Wagner, "Thixotropy," *Advances in colloid and interface science*, vol. 147, pp. 214–227, 2009.

[31] R. G. Larson and Y. Wei, "A review of thixotropy and its rheological modeling," *Journal of Rheology*, vol. 63, no. 3, pp. 477–501, 2019.

[32] K. Dullaert and J. Mewis, "A structural kinetics model for thixotropy," *Journal of non-newtonian fluid mechanics*, vol. 139, no. 1-2, pp. 21–30, 2006.

[33] D. Cheng, "Thixotropy.," *International journal of cosmetic science*, vol. 9, no. 4, pp. 151–191, 1987.

[34] C. F. Goodeve, "A general theory of thixotropy and viscosity," *Transactions of the Faraday Society*, vol. 35, pp. 342–358, 1939.

[35] M. Fazilati, S. Ingelsten, S. Wojno, T. Nypelö, and R. Kádár, "Thixotropy of cellulose nanocrystal suspensions," *Journal of Rheology*, vol. 65, no. 5, pp. 1035–1052, 2021.

[36] T. Mezger, *The rheology handbook: for users of rotational and oscillatory rheometers*. European Coatings, 2020.

[37] A. Ahmadpour and K. Sadeghy, "An exact solution for laminar, unidirectional flow of houska thixotropic fluids in a circular pipe," *Journal of Non-Newtonian Fluid Mechanics*, vol. 194, pp. 23–31, 2013.

[38] E. A. Toorman, "Modelling the thixotropic behaviour of dense cohesive sediment suspensions," *Rheologica Acta*, vol. 36, no. 1, pp. 56–65, 1997.

[39] K. L. Pinder, "Time dependent rheology of the tetrahydrofuran-hydrogen sulphide gas hydrate slurry," *The Canadian Journal of Chemical Engineering*, vol. 42, no. 3, pp. 132–138, 1964.

[40] T. Bénézech and J. F. Maingonnat, "Flow properties of stirred yoghurt: Structural parameter approach in describing time-dependency," *Journal of Texture Studies*, vol. 24, no. 4, pp. 455–473, 1993.

[41] Y. Wei, M. J. Solomon, and R. G. Larson, "A multimode structural kinetics constitutive equation for the transient rheology of thixotropic elasto-viscoplastic fluids," *Journal of Rheology*, vol. 62, no. 1, pp. 321–342, 2018.

[42] C. J. Dimitriou and G. H. McKinley, "A comprehensive constitutive law for waxy crude oil: A thixotropic yield stress fluid," *Soft Matter*, vol. 10, no. 35, pp. 6619–6644, 2014.

[43] E. J. W. Verwey, "Theory of the stability of lyophobic colloids.," *The Journal of Physical Chemistry*, vol. 51, no. 3, pp. 631–636, 1947.

[44] J. N. Israelachvili, *Intermolecular and surface forces*. Academic press, 2011.

[45] R. J. Hunter, L. R. White, and D. Y. C. Chan, *Foundations of Colloid Science*. Oxford: Oxford University Press, 1987, ISBN: 9780198553892.

[46] W. B. Russel, W. Russel, D. A. Saville, and W. R. Schowalter, *Colloidal dispersions*. Cambridge university press, 1991.

[47] P. N. Pusey and W. Van Megen, "Phase behaviour of concentrated suspensions of nearly hard colloidal spheres," *Nature*, vol. 320, no. 6060, pp. 340–342, 1986.

[48] E. Zaccarelli, "Colloidal gels: Equilibrium and non-equilibrium routes," *Journal of Physics: Condensed Matter*, vol. 19, no. 32, p. 323 101, 2007.

[49] P. J. Lu, E. Zaccarelli, F. Ciulla, A. B. Schofield, F. Sciortino, and D. A. Weitz, "Gelation of particles with short-range attraction," *Nature*, vol. 453, no. 7194, pp. 499–503, 2008.

[50] K. Hornik, M. Stinchcombe, and H. White, "Multilayer feedforward networks are universal approximators," *Neural networks*, vol. 2, no. 5, pp. 359–366, 1989.

[51] I. Goodfellow, Y. Bengio, A. Courville, and Y. Bengio, *Deep learning*. MIT press Cambridge, 2016, vol. 1.

[52] G. Cybenko, "Approximation by superpositions of a sigmoidal function," *Mathematics of control, signals and systems*, vol. 2, no. 4, pp. 303–314, 1989.

[53] S. Haykin, *Neural networks and learning machines, 3/E*. Pearson Education India, 2009.

[54] V. Nair and G. E. Hinton, "Rectified linear units improve restricted boltzmann machines," in *Proceedings of the 27th international conference on machine learning (ICML-10)*, 2010, pp. 807–814.

[55] M. Mahmoudabadbozchelou and S. Jamali, "Rheology-informed neural networks (rhinns) for forward and inverse metamodelling of complex fluids," *Scientific reports*, vol. 11, no. 1, p. 12 015, 2021.

[56] M. Mahmoudabadbozchelou, K. M. Kamani, S. A. Rogers, and S. Jamali, "Unbiased construction of constitutive relations for soft materials from experiments via rheology-informed neural networks," *Proceedings of the National Academy of Sciences*, vol. 121, no. 2, e2313658121, 2024.

[57] K. Amini et al., "Scaling laws for near-wall flows of thixo-elasto-viscoplastic fluids in a millifluidic channel," *Physics of Fluids*, vol. 36, no. 2, 2024.

[58] A. A. Mishra, A. Mark, D. Arlov, and R. Kadár, "Pipe flow of thixotropic fluids: Experiments, simulations and neural networks," Manuscript under review in Engineering Applications of Artificial Intelligence, 2025.

[59] A. A. Mishra et al., "Tunable elasto-viscoplastic properties of polymer blends for 3d printing applications," *Macromolecular Rapid Communications*, e00249, 2025.

[60] S. Zade, T. J. Shamu, F. Lundell, and L. Brandt, "Finite-size spherical particles in a square duct flow of an elastoviscoplastic fluid: An experimental study," *Journal of Fluid Mechanics*, vol. 883, A6, 2020.

[61] A. A. Mishra, V. Ghai, V. Matovic, D. Arlov, and R. Kádár, "One test to predict them all: Rheological characterization of complex fluids via artificial neural network," *Engineering Applications of Artificial Intelligence*, vol. 139, p. 109 598, 2025.

[62] A. A. Mishra et al., "The complex shear time response of saliva in healthy individuals," *Physics of fluids*, vol. 37, no. 1, 2025.

[63] R. Ghanbari et al., "Propagation of orientation across lengthscales in sheared self-assembling hierarchical suspensions via rheo-pli-saxs," *Advanced Science*, vol. 12, no. 7, p. 2 410 920, 2025.

[64] A. Pincot and M. Armstrong, "Novel tensorial thixo-visco-plastic framework for rheological characterization of human blood," *Scientific Reports*, vol. 11, no. 1, p. 22 004, 2021.

[65] T. E. Daniels and P. C. Fox, "Salivary and oral components of sjögren's syndrome," *Rheumatic Disease Clinics of North America*, vol. 18, no. 3, pp. 571–589, 1992.

[66] A. M. Frydrych, "Dry mouth: Xerostomia and salivary gland hypofunction," *Australian family physician*, vol. 45, no. 7, pp. 488–492, 2016.

[67] H.-J. Guchelaar, A. Vermes, and J. Meerwaldt, "Radiation-induced xerostomia: Pathophysiology, clinical course and supportive treatment," *Supportive care in cancer*, vol. 5, no. 4, pp. 281–288, 1997.

[68] I. H. Valdez, J. C. Atkinson, J. A. Ship, and P. C. Fox, "Major salivary gland function in patients with radiation-induced xerostomia: Flow rates and sialochemistry," *International Journal of Radiation Oncology* Biology* Physics*, vol. 25, no. 1, pp. 41–47, 1993.

[69] I. D. Mandel, A. Kutscher, C. R. Denning, R. H. Thompson, and E. V. Zegarelli, "Salivary studies in cystic fibrosis," *American journal of diseases of children*, vol. 113, no. 4, pp. 431–438, 1967.

[70] B. Satish, P. Srikala, B. Maharudrappa, S. M. Awanti, P. Kumar, and D. Hugar, "Saliva: A tool in assessing glucose levels in diabetes mellitus," *Journal of international oral health: JIOH*, vol. 6, no. 2, p. 114, 2014.

[71] Y. Hassona and C. Scully, "Salivary changes in oral mucosal diseases," *Periodontology 2000*, vol. 70, no. 1, pp. 111–127, 2016.

[72] E. Martina, A. Campanati, F. Diotallevi, and A. Offidani, "Saliva and oral diseases," *Journal of clinical medicine*, vol. 9, no. 2, p. 466, 2020.

Acknowledgments

First and foremost, I would like to express my deepest gratitude to Prof. Roland Kádár, my main supervisor. Thank you for your unwavering support, insightful guidance, and for continuously challenging me to grow as a researcher. I am especially grateful for the scientific freedom and encouragement you gave me to explore new avenues and ideas on my own—even when they seemed a bit crazy. Your scientific rigor, patience, and trust have shaped this thesis profoundly, and I am truly thankful for the countless discussions and opportunities that helped me develop as a scientist. I would also like to sincerely thank Dr. Dragana Arlov, my co-supervisor from Tetra Pak Processing Systems. Your expertise, enthusiasm, and industry-driven perspective have been invaluable throughout this project. You have motivated me to look at real-world problems through a fine scientific lens, and I am deeply grateful for your constructive feedback, mentorship, and continuous encouragement. A special and heartfelt acknowledgment goes to the late Dr. Fredrik Innings, whose vision and early guidance contributed to shaping this PhD project. His ideas and scientific curiosity continue to inspire this work, and it has been an honor to build upon his legacy. I gratefully acknowledge the financial support from the Marie Skłodowska-Curie Horizon 2020 ITN network, and I thank all members of the consortium for the stimulating discussions, training events, and collaborative spirit. My sincere thanks go to Chalmers University of Technology and the Department of Industrial and Materials Science (IMS) for providing an inspiring research environment. I am also grateful to Prof. Christer Persson for his support and for ensuring excellent conditions for my doctoral studies. To the Rheology and Soft Matter group, thank you for the collaborative atmosphere, insightful discussions, and support during experiments. Working alongside such dedicated colleagues has been a privilege. I would also like to thank all collaborators at Chalmers and beyond for their

expertise and generosity with their time. My appreciation extends as well to the master's students and research assistants I had the pleasure to supervise. Their curiosity and hard work contributed greatly to this thesis. Finally, I am deeply grateful to my parents, who have always motivated me to strive for the extraordinary, and to my family and friends for their unconditional love, encouragement, and belief in me throughout this journey. Your support has meant everything.

List of Publications

This doctoral thesis is based on the following publications:

[**Paper I**] "Scaling laws for near-wall flows of thixo-elasto-viscoplastic fluids in a millifluidic channel". Kasra Amini*, **Ases Akas Mishra***, Amit Kumar Sivakumar, Dragana Arlov, Fredrik Innings, Roland Kádár, Outi Tammisola, Fredrik Lundell. Physics of Fluids 36, 023107 (2024). (*Co-First Authors)

[**Paper II**] "One test to predict them all: Rheological characterization of complex fluids via artificial neural network". **Ases Akas Mishra**, Viney Ghai, Valentina Matovic, Dragana Arlov, Roland Kádár. Engineering Applications of Artificial Intelligence 139, 109598 (2025)

[**Paper III**] "Pipe Flow of Thixotropic Fluids: Experiments, Simulations and Neural Networks". **Ases Akas Mishra**, Andreas Mark, Dragana Arlov, Roland Kádár. Manuscript submitted.

[**Paper IV**] "Tunable Elasto-Viscoplastic Properties of Polymer Blends for 3D Printing Applications". **Ases Akas Mishra**, Manoj Chandregowda, Janina Faiß, Marko Bek, Ann E.Terry, Kim Nygård, Dragana Arlov, Roland Kádár . Macromolecular Rapid Communications, 0:e00249 (2025)

[**Paper V**] "The complex shear time response of saliva in healthy individuals". **Ases Akas Mishra**, Ulrica Almhöjd, Hülya Çevik-Aras, Amela Fisic, Richard Olofsson, Annica Almståhl, Roland Kádár. Physics of Fluids 37, 011911 (2025)

Contribution report
Paper I: Main author (Co-First Author). The author planned and executed all the experimental work, and data analysis of the results together with K.A. The author wrote the manuscript with input from the other co-authors.

Paper II: Main author. The author planned and executed all the experimental work and data analysis of the results. The neural networks was implemented together with V.M. The author wrote the manuscript with input from the other co-authors.
Paper III: Main author. The author planned and executed all the experimental work, data analysis of the results, simulation, and neural networks. The author wrote the manuscript with input from the other co-authors.
Paper IV: Main author. The author planned and executed all the experimental work, data analysis of the results, and simulations. The author wrote the manuscript with input from the other co-authors.
Paper V: Main author. Saliva samples were collected and their physiochemistry was analyzed by collaborators at Sahlgrenska Academy (U.A., H.C., A.F., R.O., and A.A.). The author planned and executed the rheological experimental work, and data analysis of the results together with R.K. The author wrote the manuscript with input from the other co-authors.

Other publications not included in this thesis:

[1] "Halbach Array Induced Magnetic Field Alignment in Boron Nitride Nanocomposites", V. Ghai, **A. A. Mishra**, E. Huang, R. Ngaloy, S. P. Dash, A. Matic, R. Kádár. Advanced Science, 12 (6), 2408532 (2025)

[2] "A novel 3D printed hierachical nanocomposite for antibacterial and bio/wearable electronics applications", **A. A. Mishra**, V. Ghai, S. Pandit, I. Mijakovic, R. Kádár. Manuscript Submitted, Available at SSRN 5706802

[3] "Topology-Driven Flow Alignment in Surface-Modified Cellulose Nanocrystals via Rheo-PLI-SAXS Study", A. Sonker, **A. A. Mishra**, K. Sekar, M. Bek, A. Terry, K. Nygård, S. Ansell, G. Westman, R. Kádár. Manuscript Submitted

[4] "3D Bioprinting of Yeast Bioreactors Using Optically Active Nano-Cellulose", **A. A. Mishra**, S. M. Calvo, K. Sekar, V. Ghai, V. Siewers, M. Chandregowda, S. Pandit, I. Mijakovic, R. Kádár. Manuscript

[5] "Yielding Dynamics of Cellulose Nanocrystals via Rheo-Polarised Light Imaging", **A. A. Mishra**, K. Sekar, R. Kádár. Manuscript